AD-A205 187

FILE COPY

(2)

AFOSR-TR- 89-0230

An Annual Report
Contract No. AFOSR-87-0082-A
January 1, 1988 - December 31, 1988

PROCESSING AND PROPERTIES OF ADVANCED ALUMINUM ALLOYS

Submitted to:

Air Force Office of Scientific Research/NE
Building 410
Bolling Air Force Base
Washington, D.C. 20332
Attention: Dr. Alan H. Rosenstein

Submitted by:

J.A. Wert
Associate Professor

E.A. Starke, Jr.
Earnest Oglesby Professor of
Materials Science and Dean

Report No. UVA/525671/MS89/101
February 1989

Approved for public release;
distribution unlimited.

AFOSR/XOTD
Building 410
[illegible] 20332-6448

[illegible] Information Division

SCHOOL OF ENGINEERING AND
APPLIED SCIENCE

Department of Materials Science

UNIVERSITY OF VIRGINIA
CHARLOTTESVILLE, VIRGINIA 22901

DTIC
ELECTE
MAR 06 1989
S D
H

UNIVERSITY OF VIRGINIA
School of Engineering and Applied Science

The University of Virginia's School of Engineering and Applied Science has an undergraduate enrollment of approximately 1,500 students with a graduate enrollment of approximately 600. There are 160 faculty members, a majority of whom conduct research in addition to teaching.

Research is a vital part of the educational program and interests parallel academic specialties. These range from the classical engineering disciplines of Chemical, Civil, Electrical, and Mechanical and Aerospace to newer, more specialized fields of Applied Mechanics, Biomedical Engineering, Systems Engineering, Materials Science, Nuclear Engineering and Engineering Physics, Applied Mathematics and Computer Science. Within these disciplines there are well equipped laboratories for conducting highly specialized research. All departments offer the doctorate; Biomedical and Materials Science grant only graduate degrees. In addition, courses in the humanities are offered within the School.

The University of Virginia (which includes approximately 2,000 faculty and a total of full-time student enrollment of about 17,000), also offers professional degrees under the schools of Architecture, Law, Medicine, Nursing, Commerce, Business Administration, and Education. In addition, the College of Arts and Sciences houses departments of Mathematics, Physics, Chemistry and others relevant to the engineering research program. The School of Engineering and Applied Science is an integral part of this University community which provides opportunities for interdisciplinary work in pursuit of the basic goals of education, research, and public service.

ANNUAL REPORT

Contract No. AFOSR-87-0082-A
January 1, 1988 - December 31, 1988

PROCESSING AND PROPERTIES OF ADVANCED ALUMINUM ALLOYS

Submitted to:

Air Force Office of Scientific Research/NE
Building 410
Bolling Air Force Base
Washington, D.C. 20332

Attention: Dr. Alan H. Rosenstein

Submitted by:

John A. Wert
Associate Professor

Edgar A. Starke, Jr.
Earnest Oglesby Professor of
Materials Science and Dean

Department of Materials Science

SCHOOL OF ENGINEERING AND APPLIED SCIENCE

UNIVERSITY OF VIRGINIA

CHARLOTTESVILLE, VIRGINIA

Report No. UVA/525671/MS89/101
February 1989

UNCLASSIFIED

SECURITY CLASSIFICATION OF THIS PAGE

REPORT DOCUMENTATION PAGE

Form Approved OMB No. 0704-0188

1a. REPORT SECURITY CLASSIFICATION
Unclassified

1b. RESTRICTIVE MARKINGS
None

2a. SECURITY CLASSIFICATION AUTHORITY

2b. DECLASSIFICATION / DOWNGRADING SCHEDULE

3. DISTRIBUTION / AVAILABILITY OF REPORT
Approved for public release;
distribution unlimited.

4. PERFORMING ORGANIZATION REPORT NUMBER(S)
UVA/525671/MS89/101

5. MONITORING ORGANIZATION REPORT NUMBER(S)
AFOSR-TR- 89-0230

6a. NAME OF PERFORMING ORGANIZATION
University of Virginia
Department of Materials Science

6b. OFFICE SYMBOL *(If applicable)*

7a. NAME OF MONITORING ORGANIZATION
Air Force Office of Scientific Research/PKD

6c. ADDRESS *(City, State, and ZIP Code)*
Department of Materials Science
Thornton Hall
Charlottesville, VA 22901

7b. ADDRESS *(City, State, and ZIP Code)*
Building 410
Bolling Air Force Base
Washington, D.C. 20332-6448

8a. NAME OF FUNDING / SPONSORING ORGANIZATION
AFOSR/NE

8b. OFFICE SYMBOL *(If applicable)*
NE

9. PROCUREMENT INSTRUMENT IDENTIFICATION NUMBER
AFOSR-87-0082-A

8c. ADDRESS *(City, State, and ZIP Code)*
Building 410
Bolling Air Force Base
Washington, D.C. 20332-6448

10. SOURCE OF FUNDING NUMBERS

PROGRAM ELEMENT NO.	PROJECT NO.	TASK NO.	WORK UNIT ACCESSION NO.
61102F	2306	A1	

11. TITLE *(Include Security Classification)*
Processing and Properties of Advanced Aluminum Alloys

12. PERSONAL AUTHOR(S)
J.A. Wert and E.A. Starke, Jr.

13a. TYPE OF REPORT
Annual

13b. TIME COVERED
FROM 1/1/88 TO 12/31/88

14. DATE OF REPORT *(Year, Month, Day)*
February 1989

15. PAGE COUNT
78

16. SUPPLEMENTARY NOTATION

17. COSATI CODES

FIELD	GROUP	SUB-GROUP

18. SUBJECT TERMS *(Continue on reverse if necessary and identify by block number)*

19. ABSTRACT *(Continue on reverse if necessary and identify by block number)*

This project has as its focus microstructure control for improving fracture resistance of advanced aluminum alloys. Our progress report is divided into two major parts: Part I which is concerned with the quench sensitivity of the Al-Li-Cu-Mg alloy 2090 and the effect of quench rate on fracture behavior, and Part II which is concerned with the recovery and recrystallization mechanisms that occur in an alloy having a high density of dispersoid particles. The grain size of aluminum alloys can affect both strength and deformation behavior and often controls the degree of superplasticity during elevated temperature deformation.

Continued on Page iii

20. DISTRIBUTION / AVAILABILITY OF ABSTRACT
☒ UNCLASSIFIED/UNLIMITED ☐ SAME AS RPT. ☐ DTIC USERS

21. ABSTRACT SECURITY CLASSIFICATION
Unclassified

22a. NAME OF RESPONSIBLE INDIVIDUAL
Alan H. Rosenstein

22b. TELEPHONE *(Include Area Code)*
(202) 767-49~~84~~ 33

22c. OFFICE SYMBOL
NE

DD Form 1473, JUN 86 *Previous editions are obsolete.*

SECURITY CLASSIFICATION OF THIS PAGE
Unclassified

The quench sensitivity of aluminum alloys often determines their usefulness in thick section applications. The new Al-Li-Cu-Mg alloy, 8090, is being considered for large forgings in advanced aerospace systems. Time-temperature-transformation diagrams were developed for precipitation of the equilibrium $T_2(Al_6CuLi_3)$ and $S(Al_2CuMg)$ phases in two compositional variations of the Al-Li-Cu-Mg alloy 8090. The start of T_2 nucleation proved to be relatively rapid in both alloy variants with T_2 nucleating in under five seconds at $400^\circ C$-$450^\circ C$ in the more heavily alloyed material. Nucleation of the T_2 phase was not evident in the lean alloy until after 20 seconds at these temperatures. The S phase nucleation appeared to be less sensitive to the composition range studied, with its earliest appearance being after ten seconds at $300^\circ C$. The volume fraction of T_2 correlated well with Charpy energy absorption values, with increasing amounts of T_2 leading to decreasing toughness. 8090, like many other Al-Li-X alloys, is quench sensitive, requiring fairly rapid cooling rates from the solutionizing temperature for mechanical property optimization.

Reduction of grain size in aluminum alloys can increase strength and can lead to superplasticity during elevated temperature deformation. Thermomechanical processing for grain size control relies on particle dispersions to manage relaxation (recovery and recrystallization) of the deformation substructure. This study has focused on the recovery and recrystallization mechanisms in a model alloy with composition Al-0.24Zr-0.1Si. This alloy contains a high density of dispersoid particles which provide a drag pressure on migrating boundaries sufficient to retard discontinuous recrystallization. The distribution of dispersoid particles, the deformation microstructure after cold rolling and the annealing conditions were found to be important variables affecting the recovery and recrystallization kinetics of the alloy. The results indicate how the microstructure evolves during static annealing and during concurrent annealing and elevated temperature deformation.

DTIC COPY INSPECTED

Accession For
NTIS GRA&I ☑
DTIC TAB ☐
Unannounced ☐
Justification
By
Distribution/
Availability Codes
Dist | Avail and/or Special
A-1

TABLE OF CONTENTS

PART I. Quench Sensitivity of the Al-Li-Cu-Mg Alloy 8090. G.N. Colvin and E.A. Starke, Jr. 1

PART II. Processing of Aluminum Alloys for Structure Control. J.A. Wert, H. Gudmundsson and D. Brooks 28

PART I. QUENCH SENSITIVITY OF THE Al-Li-Cu-Mg ALLOY 8090

G.N. Colvin and E. A. Starke, Jr.

Time-temperature-transformation diagrams were developed for precipitation of the equilibrium $T_2(Al_6CuLi_3)$ and $S(Al_2CuMg)$ phases in two compositional variations of the Al-Li-Cu-Mg alloy 8090. The start of T_2 nucleation proved to be relatively rapid in both alloy variants with T_2 nucleating in under five seconds at 400°C-450°C in the more heavily alloyed material. Nucleation of the T_2 phase was not evident in the lean alloy until after 20 seconds at these temperatures. The S phase nucleation appeared to be less sensitive to the composition range studied, with its earliest appearance being after ten seconds at 300°C. The volume fraction of T_2 correlated well with Charpy energy absorption values, with increasing amounts of T_2 leading to decreasing toughness. 8090, like many other Al-Li-X alloys, is quench sensitive, requiring fairly rapid cooling rates from the solutionizing temperature for mechanical property optimization.

1. Introduction

The primary purpose of quenching age-hardened aluminum alloys is to maintain a large degree of supersaturation of solute atoms homogeneously distributed in solid solution. This permits precipitation of an optimum concentration and distribution of hardening particles during the aging treatment. As quench rates decrease, more time is allowed for solute atoms to migrate to grain boundaries or precipitate as matrix phases. Grain boundaries act as heterogeneous nucleation sites by reducing the free energy barrier to nucleation (1). When thermodynamic and kinetic demands are satisfied, precipitation can occur along the grain boundary and subsequently enhance intergranular cracking, grain boundary decohesion and premature material failure (2).

It has been well established that deformation of Al-Li-X alloys occurs by planar slip due to the coherent nature of the primary strengthener: delta prime (Al_3Li) (3,4). Planar slip concentrates stress at grain boundaries and may prematurely nucleate cracks and cause early failure. Failure may occur transgranularly along slip bands or intergranularly along grain boundaries. Grain boundary precipitates enhance void nucleation and accelerate intergranular fracture and are thus a very important contributor to the low resistance to fracture often observed in Al-Li-X alloys (5). This report section describes the influence of quench rates on precipitation of the grain boundary phase $T_2(Al_6CuLi_3)$ and the equilibrium phase $S(Al_2CuMg)$ that form in the Al-Li-Cu-Mg alloy 8090 and their subsequent effects on the alloy's fracture behavior.

2. Procedures

2.1. Preliminary Experiments

The material used in this study was obtained from Alcan International Limited as two 2.54 cm thick plates in the T3 temper. One plate had a "rich" composition and one a "lean" composition but both were within the limits of alloy 8090, Table 1.

Blocks 7.6 cm X 7.6 cm X 2.54 cm were sectioned from each alloy with two holes drilled such that the temperatures of the outside surface and the interior could be measured. K-type thermocouples were inserted into each hole, assuring good thermal contact, and then were cemented into place using a high temperature ceramic. Each slab was solution heat treated at 550°C for one hour then cooled via one of three mediums: room temperature water, pure glycol polymer quenchant, or air. An oscilloscope was employed to measure and record the cooling response of each of the thermocouples. Samples of both compositions from the water quenched, polymer quenched, and still-air quenched materials were mounted using a hardener/resin epoxy system. They were hand-ground flat to 600 grit paper and polished through collodial silica using conventional techniques. The specimens were etched with water-0.25HF for 5 seconds to darken the secondary phases and examined using an oil immersion lens at a magnification of 1250X.

Eight round tensile specimens with 2.8 cm gauge lengths and 0.6 cm gauge diameters were machined from each quenched block with the gauge length of the bars machined parallel to the rolling direction of the plate. Four of the eight tensile specimens were tested in the as-quenched condition. The remaining tensile specimens were stretched and aged with one of two treatments which were reported to produce peak strengths in 8090 (6): 2% stretch + 190°C/16 hours or 4% stretch + 170°C/24 hours. Two tensile specimens from each composition/quench and aged condition were tested.

Two standard size Charpy specimens were machined from each quench condition with a V-notch in the rolling direction of the plate. These were tested by the three-point bend method employing a slow strain rate to minimize variability in the data. Energy values measured on charpy specimens are expressed as W/A values where W=energy absorbed and A=net(unnotched) section area. The energy absorbed was approximated by the area under the load/displacement curve. W/A values can be used to obtain a relative ranking of fracture resistance for a given set of specimens provided that parameters remain constant through the experiments (7).

2.2. Determination of TTT Diagrams

Specimens 7.6 cm X 2.54 cm X 0.4 cm were sectioned from each plate such that the plate's rolling direction was perpendicular to the plane of the sample. The samples were ground to a thickness of 0.3 cm in order to minimize the time required for the specimen to come to temperature when immersed in a salt bath (8). The specimens were solutionized in a salt bath at 550°C for one hour, immersed into an adjacent salt bath for the appropriate isothermal hold temperature and time, then quenched into an ice-brine solution.

Optical microscopy was used as a rapid means of determining the effect of time at temperature on the microstructure of each composition. Sections were cut from each of the heat treated specimens then mounted and polished using the technique described previously. The Guinier x-ray diffraction method was used to precisely determine the phases present for each time/temperature condition. Specimens were cut to 0.05 cm thick using a slow speed diamond saw and then ground to remove the deformation associated with sawing. The foils were irradiated in an evacuated Guinier camera for 100 hours using Cu K-α radiation. Phase identifications were made by measuring the d-spacings of the diffraction lines and comparing these to powder diffraction card files. Transmission electron microscopy (TEM) was also utilized to confirm the presence of the various phases identified by x-ray diffraction. Samples were prepared for scanning electron microscopy (SEM) examination by etching with boiling 9:1 methanol:bromine solution which selectively removes the aluminum matrix leaving the precipitated particles in relief. Optimum etching time varied from 30 seconds to 1 minute. The volume percent of secondary phases was measured using a quantitative analysis program in conjunction with an SEM. This analysis was typically performed between 1000-5000X magnification depending upon the precipitate size and distribution. In samples where both T_2 and S phases were present the separate volume fraction of each phase was obtained. The T_2 and S phases were identified through EDAX and their volume fractions were determined and separated by the quantitative metallography program which used their respective characteristic reflectivities.

The small sample size necessary for isothermal treatment prohibited K_{IC} determination as a function of time at temperature. Consequently, the fracture characteristics of the two alloys were evaluated using three-point slow bend Charpy tests. One primary difficulty with this technique is that the relatively blunt notch radius of the standard V-notch Charpy specimen can postpone the onset of crack extension to higher apparent toughness values. This permits general yielding to occur prior to fracture (7). To minimize this effect the V-notch radius was machined as sharp as possible using a specially ground carbide tool with a radius of less than 0.0025 cm.

Two Charpy specimens were machined from the isothermally heat treated specimens for the conditions listed in Table 2. Due to the necessary thinness of the plates (0.3 cm) the thickness of the Charpy specimens did not meet ASTM standards. A 0.05 cm deep V-notch was machined parallel to the rolling direction of the as-received plate material. A MTS servohydraulic tensile testing machine was used with a three point bend apparatus to obtain load versus strain curves. The bend apparatus was set up with frictionless rollers and alignment according to ASTM E812-81 requirements (9).

3. Results and Discussion

3.1. Preliminary Experiments

Cooling curves for each composition and quench method are shown in Figures 1 and 2. Water quenching resulted in cooling rates of approximately 150°C/sec, the polymer quench a cooling rate of approximately 9°C/second and the air quench a cooling rate of approximately 0.2°C/sec for the sample size used. Water quenching cooled the centerline of the blocks to below 200°C in under 3.5 seconds. The cooling response produced by water quenching resembles results determined by several researchers on water quenching of aluminum alloys, verifying the accuracy of the experimental setup employed in these investigations (10,11). Polymer quenching cooled the specimen to 250°C in 10 seconds; however, the cooling rate decreased in the region from 250°C to 200°C. This is a characteristic of polymer quenches which are designed to reduce the degree of distortion during quenching (11). Large Fe and Si-rich phases, that form during solidification and thus are present in the as-received material, were the only precipitates observed optically in material that was water quenched; however, light gray, matrix and grain boundary precipitates were evident in the slower cooled material, illustrating the quench sensitivity of the 8090 alloy, Figure 1. Cooling at 150°C/sec (water quench) and 9°C/sec (polymer quench) appeared successful in minimizing precipitation in the lean composition, Figure 1; however, the slow cooling rate of the air quench (0.2°C/sec) permitted both grain boundary and matrix precipitation. In the rich alloy only 150°C/sec (water quench) was sufficient to prevent such precipitation, Figure 2. These results illustrate the significant influence that minor variations in composition have on the quench sensitivity of 8090.

Results of the tensile tests for the as-quenched specimens are listed in Table 2. As expected, the rich composition produced higher strengths than measured for the lean alloy. This difference is associated more with Al_3Li precipitation than with precipitation of T_2 and S. It is difficult to suppress Al_3Li precipitation in any Al-Li alloy containing more than 1 wt% lithium. The higher lithium content of the rich composition promoted a greater volume fraction of the Al_3Li strengthening phase. Slower cooling rates produced greater as-quenched strengths in both materials since more time was available at intermediate temperatures for the precipitation of other hardening phases such as S'.

Results for the aged tensile specimens are also listed in Table 2. The rich composition consistently exhibited ultimate and yield strengths superior to those produced by the lean alloy. The rich alloy's higher lithium and copper contents promoted precipitation of higher volume fractions of hardening phases during aging. In contrast to the as-quenched results the fastest cooling rates (water quenching) promoted the greatest strengths for the aged specimens. The faster cooling rates quenched in more solute which was then available to form strengthening precipitates during aging.

Charpy energy absorption values are shown in Figure 3. As quench rates increased, the energy absorbed or resistance to crack propagation improved for both compositions. This is primarily due to the greater success in suppressing grain boundary precipitation by the faster quenching methods. For both alloys, cooling at $150^{\circ}C$/sec. (water quench) produced the greatest resistance to crack propagation, and $0.2^{\circ}C$/sec. (air cool) promoted the least resistance to crack propagation. However, a quench rate of $9^{\circ}C$/sec. (polymer quench) was more successful in maintaining fracture resistance in the lean alloy than occurred for the rich alloy. This is evidence that a critical cooling rate must be achieved to effectively suppress precipitation during the quench in order to optimize mechanical properties and illustrates that lean alloys should be selected for thick plate or heavy sections.

3.2. Determination of TTT Diagrams

Optical microscopy was used in conjunction with x-ray diffraction and transmission electron microscopy to determine, quantitatively, the volume fraction of phases present after various thermal treatments. This data was used to plot time-temperature-transformation (TTT) diagrams. Representative optical micrographs of the rich and lean alloys showing both matrix and grain boundary precipitates are given in Figure 4. These precipitates were identified by x-ray analysis as T_2 and S. The T_2 phase heterogeneously nucleates at grain boundaries in Al-Li-Cu alloys (12). It is a member of a group of quasi-crystals which have been under intense study during the past several years (13) and is believed to possess an icosahedral structure with 5-fold diffraction symmetry. The S phase is present in many commercial Al-Cu-Mg alloys.

The phase boundaries for the start of T_2 and S nucleation, as determined in this study, are shown in Figures 5 and 6. The T_2 phase precipitated at 400°C-450°C after only 5 seconds in the rich alloy. The relatively rapid precipitation of T_2 is an indication of a low free energy barrier ΔG^* to nucleation. T_2 heterogeneously nucleates on high angle grain boundaries -- an imperfection which reduces ΔG^* by providing a portion of the interfacial energy needed to accomplish the nucleation process (1).

The TTT curve for T_2 for the lean composition alloy was shifted to longer hold times (nucleation of the T_2 phase was not apparent until approximately 20 seconds at 400°C-450°C); however, the curve exhibited the same general shape as that of the rich alloy. The lean alloy's lower lithium and copper contents decrease ΔG_v, the volume free energy change since ΔG_v is proportional to the concentration of solute (1). Consequently, the driving force for nucleation is decreased, and precipitation is delayed.

It was more difficult to establish phase boundaries for S nucleation. Guinier diffraction identified S at longer hold times (300°C/1000 sec); however, at shorter times where optical metallography showed precipitation, Guinier diffraction analysis was inconclusive in identifying the presence of S. At these lower volume fractions TEM was used to positively identify S. Phase boundaries for S proved to be very similiar for both compositions with Al_2CuMg nucleating within 10 seconds at 300°C-350°C. Apparently the increased copper content of the rich alloy did not significantly reduce the free energy barrier for nucleation of S. The magnesium content, which was the same for both alloys, most probably controls the nucleation rate for this precipitate for the compositional range studied.

A typical microstructure as revealed by etching with the bromine:methanol solution is shown in Figure 7. Quantitative analysis verified that T_2 volume fractions increased during the isothermal heat treatments. The T_2 volume fraction in the rich alloy was almost double that for the lean material after 450°C/1000 sec, Figure 8. The T_2 volume fractions were greatest for both alloys at temperatures higher than the nose of the TTT curve. This may be due to the competition in nucleation and growth between the S and T_2 phases at intermediate temperatures. If the growth of S ties up a significant fraction of the copper solute, then growth of T_2 may be decreased at these temperatures. The volume fraction of S increased during the isothermal hold with the greatest percentages of S occurring at 350°C for both compositions, Figure 8. The rich alloy had volume fractions of both T_2 and S substantially greater than those for the lean composition.

Results of the Charpy tests are listed in Table 2. A decrease in the charpy energy absorbed (area under the load/deformation curve) was observed after only 5 seconds at 450°C-400C for the rich alloy. This is an indication of a loss in resistance to crack propagation and correlates well with the optical microscopy and Guinier diffraction analysis which indicated T_2 precipitation within 5 seconds at these temperatures, Figure 9. Charpy values, after holding 2 seconds at 450°C-400°C, were the same as the water quenched results, indicating that significant nucleation/growth of T_2 occurred during the time interval of 2-5 seconds. Energy absorption values continued to decrease to hold times of 100 sec., after which an increase was observed for times up to 1000 sec. The T_2 phase controls the fracture behavior from 0 to 100 sec. by promoting cracks along grain boundaries and reducing toughness. At longer hold times S co-precipitates in the matrix and along subgrain boundaries. The S precipitates homogenize slip in the matrix as dislocations bypass or loop around these particles. This reduces the stress at the grain boundaries, which in turn reduces the deleterious effect of T_2 precipitation. The result is an increase in fracture resistance as isothermal hold times increase from 100 to 1000 seconds. The effect of slip homogenization on decreasing the deleterious effect of grain boundary precipitation in Al-Li alloys has been described by Cassada et al. (14).

After 10 seconds at isothermal hold temperatures of 450°C-300°C, no significant decrease in Charpy energy absorption was observed for the lean alloy. This indicates that precipitation of secondary phases does not occur in this alloy until after 10 seconds, which is consistent with metallographic observations. The pattern of initial loss of fracture toughness (caused by growth of T_2) followed by increasing fracture toughness (promoted by S precipitation) was duplicated with the lean alloy.

The fracture mode of the Charpy specimens was predominantly intergranular following treatments at higher temperatures (450°C-400°C) and shorter hold times (<100 seconds). The percentage of intergranular fracture increased with increasing hold times up to 100 seconds, Figure 10. This evolution in fracture mode corresponds to growth of T_2 along high angle grain boundaries. Stable T_2 particles nucleated cracks along grain boundaries resulting in marked reductions in fracture resistance. Cross sections through the fracture surface show the crack path preferentially following high angle grain boundaries. The jagged morphology of the primary crack is apparent as are secondary cracks at right angles to the primary crack which corresponds to delamination along the high angle boundaries.

As hold times at 400°C increased from 100 sec. to 1000 sec., a change in fracture mode occurred. Dimpled transgranular fracture surfaces, evidence of microvoid growth and coalescence, were apparent in samples held for 1000 seconds at 400°C-350°C for both compositions, Figure 10. Apparently the growth of S during this time interval resulted in increased homogenization of slip, reducing the stress concentrated at the grain boundaries but enhancing void nucleation and growth at the matrix/precipitate interface. The size of the dimples observed after 1000 seconds decreased as the temperatures decreased relating directly to the size of the S phase. This higher energy fracture mode improved the fracture toughness. These results illustrate the importance of minimizing strain localization as a method of improving the fracture toughness in alloys containing a significant amount of grain boundary precipitates.

The results of this study demonstrate a good correspondence between loss of fracture resistance and an increase in volume fraction and growth of T_2 and S. The most rapid loss in fracture resistance for both alloys occurred at higher temperatures (400°C-450°C) where T_2 was the dominant precipitate. However, large decreases in properties also occurred in the temperature range of 300°C-250°C where the S phase dominated. Obviously, the S phase has both beneficial and deleterious effects. Depending on its size and spacing it can homogenize slip to reduce the adverse effect of large T_2 grain boundary precipitates. However, since the precipitate is not sheared by dislocations, voids can nucleate at the matrix/particle interface. As the spacing between particles decreases (which occurs as the temperature is reduced) void coalescence is enhanced and the fracture resistance decreases. The rapid precipitation of T_2 for the composition variations of 8090 is an indication of the relatively quench sensitive nature of the alloy. Al-2.58Li-1.36Cu-0.86Mg-0.13Zr requires a cooling rate greater than 30°C/sec from 550°C-250°C to bypass the nose of the T_2 and S C-curves and avoid nucleation of these equilibrium phases. Al-2.28Li-0.86Cu-0.90Mg-0.13Zr requires a quench rate > 13°C/sec through the same temperature range to avoid T_2 and S precipitation and thereby optimize mechanical properties. In an industrial environment where conditions are not ideal, a large 8090 plate could easily be subjected to quench rates slower than those required for suppressing formation of T_2 and S, resulting in lower mechanical properties. Consequently, post-quenching aging treatments must be designed to minimize the adverse effect of the grain boundary precipitates.

4. Conclusions

The rate of quenching after solution treatment does influence the mechanical properties of 8090. A cooling rate of 150°C/sec was sufficient to suppress deleterious nucleation of T_2 and S phases for the compositional variants studied. A cooling rate of 9°C/sec was adequate to suppress precipitation in the lean alloy, but was not sufficient for the rich alloy. This was reflected by a lower resistance to fracture for the slower cooling rates. The more heavily alloyed composition, Al-2.58Li-1.36Cu-0.9Mg-0.13Zr, exhibited a greater sensitivity to quenching rates than did Al-2.28Li-0.86Cu-0.9Mg-0.13Zr. This is due to the more rapid nucleation of T_2 in the rich alloy. The T_2 phase formed after 5 sec. at 400°C-450°C in the rich alloy; however, T_2 was not evident until after 20 sec. in the less heavily alloyed composition. The S phase formed after 10 sec. at 300°C-350°C in both alloys. Apparently S nucleation is insensitive to the lithium and copper difference between the alloy variants. The magnesium content, which is identical in both variants, may be the rate limiting solute addition.

A decrease of fracture resistance correlates well with the growth of T_2 precipitates indicating that T_2 is the principal cause of the loss of mechanical properties in 8090 following high temperature heat treatments. Increases in energy absorption values after longer hold times (400°C/1000 sec) occurred due to precipitation of S. The S phase homogenized slip relieving some of the detrimental influence of T_2 on grain boundary fracture.

Al-2.58Li-1.36Cu-0.86Mg-0.13Zr requires a cooling rate greater that 30°C/sec from 550°C to 250°C to suppress nucleation of equilibrium T_2 and S phases. Al-2.28Li-0.86Cu-0.90Mg-0.13Zr requires a cooling rate greater than 13°C/sec through the same temperature range for mechanical property optimization. The rapid precipitation of T_2 indicates that 8090 is relatively quench sensitive; however, T_2 can be suppressed if the above cooling rates are achieved.

5. References

1. J.W. Christian, The Theory of Transformations in Metals and Alloys, First Edition, Pergamon Press, Oxford, England (1965).

2. R.F. Ashton, D.S. Thompson, E.A. Starke, Jr., and F.S. Lin, in Aluminum-Lithium Alloys III, eds. C. Baker, P.J. Gregson, S.J. Harris and C.J. Peel, The Institute of Metals, London (1986), p. 66.

3. T.H. Sanders, Jr. and E.A. Starke, Jr., Acta Met., Vol. 30 (1982), p. 927.

4. K.V. Jata and E.A. Starke, Jr., Met. Trans. A, Vol. 17A (1986), p. 1011.

5. E.A. Starke, Jr. and F.S. Lin, Met. Trans. A, Vol. 13A (1982), p. 2259.

6. William Miller, Alcan Banbury Laboratory, United Kingdom, Private Communication, January, 1987.

7. Rapid Inexpensive Tests for Determining Fracture Toughness, National Materials Advisory Board, Washington, D.C. (1976).

8. J.T. Staley, Alcoa Technical Center, Alcoa Center, PA, Private Communication, September, 1986.

9. Slow-Bend Notched Bar Testing of Metallic Materials, American Society for Testing Materials ASTM E812-81, Philadelphia, PA, (1981).

10. C.E. Bates, T. Landig, G. Seitanakis, Quench Factor Analysis: A Powerful Tool Comes of Age, Park Chemical Company Technical Publication (June, 1986), p. 4.

11. T. Croucher and D. Butler, "Polymer Quenching of Aluminum Castings," in the Proceedings of the 26th National SAMPE Symposium (April, 1981), p. 530.

12. W.A. Cassada, G.J. Shiflet and E.A. Starke, Jr., Scripta Met., Vol. 20 (1986), p. 751.

13. B. Dubost, M. Audier, P. Jeanmart, J.M. Lang, and P. Sainfort, in Aluminum-Lithium IV, eds. G. Champier, B. Dubost, M. Miannay, L. Sabetay, Journal de Physique, C3, (1987) p. 497.

14. W.A. Cassada, G.J. Shiflet, and E.A. Starke, Jr., Acta Met., Vol. 34 (1986), p. 367.

TABLE 1. COMPOSITION OF THE VARIANTS OF 8090.

Alloy Des.	Li	Cu	Mg	Zr	Fe	Si	Al
Rich	2.58	1.36	0.89	0.13	0.17	0.04	bal
Lean	2.28	0.86	0.90	0.13	0.13	0.06	bal

TABLE 2. TENSILE DATA FOR AS-QUENCHED AND AGED CONDITIONS.

COMPOSITION	COOLING	AGING TREATMENT	UTS (MPa)	YS (MPa)	ELONG (%)
Al-2.28Li-0.86Cu -0.90Mg-0.13Zr	AIR COOL	no age	414	237	10
		2% 190°C/16h	449	401	8
		4% 170°C/24h	465	401	6
	POLYMER QUENCH	no age	393	229	17
		2% 190°C/16h	481	415	8
		4% 170°C/24h	481	415	7
	WATER QUENCH	no age	374	208	18
		2% 190°C/16h	492	428	8
		4% 170°C/24h	483	417	8
Al-2.58Li-1.36Cu -0.89Mg-0.13Zr	AIR COOL	no age	456	288	6
		2% 190°C/16h	485	417	6
		4% 170°C/24h	503	441	5
	POLYMER QUENCH	no age	450	284	11
		2% 190°C/16h	524	450	7
		4% 170°C/24h	519	451	5
	WATER QUENCH	no age	425	264	16
		2% 190°C/16h	535	464	8
		4% 170°C/24h	517	448	7

TABLE 3. CHARPY ENERGY ABSORPTION DATA.

COMPOSITION	ISOTHERMAL TEMP.	HOLD TIME(sec.)					
		2	5	10	20	100	1000
	525°C	-	-	-	-	-	4.00
AL-2.58Li-1.36Cu -0.9Mg-0.13Zr	500°C	-	-	4.65	-	4.05	2.33
	450°C	4.55	3.25	2.30	-	1.37	2.31
	400°C	4.25	3.13	1.60	-	1.35	2.30
	350°C	-	-	3.25	-	2.00	2.20
	300°C	-	-	4.45	-	0.91	1.63
	250°C	-	-	4.40	-	1.21	0.63
	200°C	-	-	-	-	-	0.33
	Water Quench						4.45
	525°C	-	-	-	-	-	4.10
Al-2.28Li-0.86Cu -0.9Mg-0.13Zr	500°C	-	-	4.58	-	3.51	3.42
	450°C	-	-	4.81	3.92	2.60	3.11
	400°C	-	-	4.84	2.50	2.74	4.31
	350°C	-	-	4.90	-	2.00	2.72
	300°C	-	-	4.77	-	1.93	1.86
	250°C	-	-	4.76	-	2.41	1.65
	200°C	-	-	-	-	-	1.01
	Water Quench						4.85

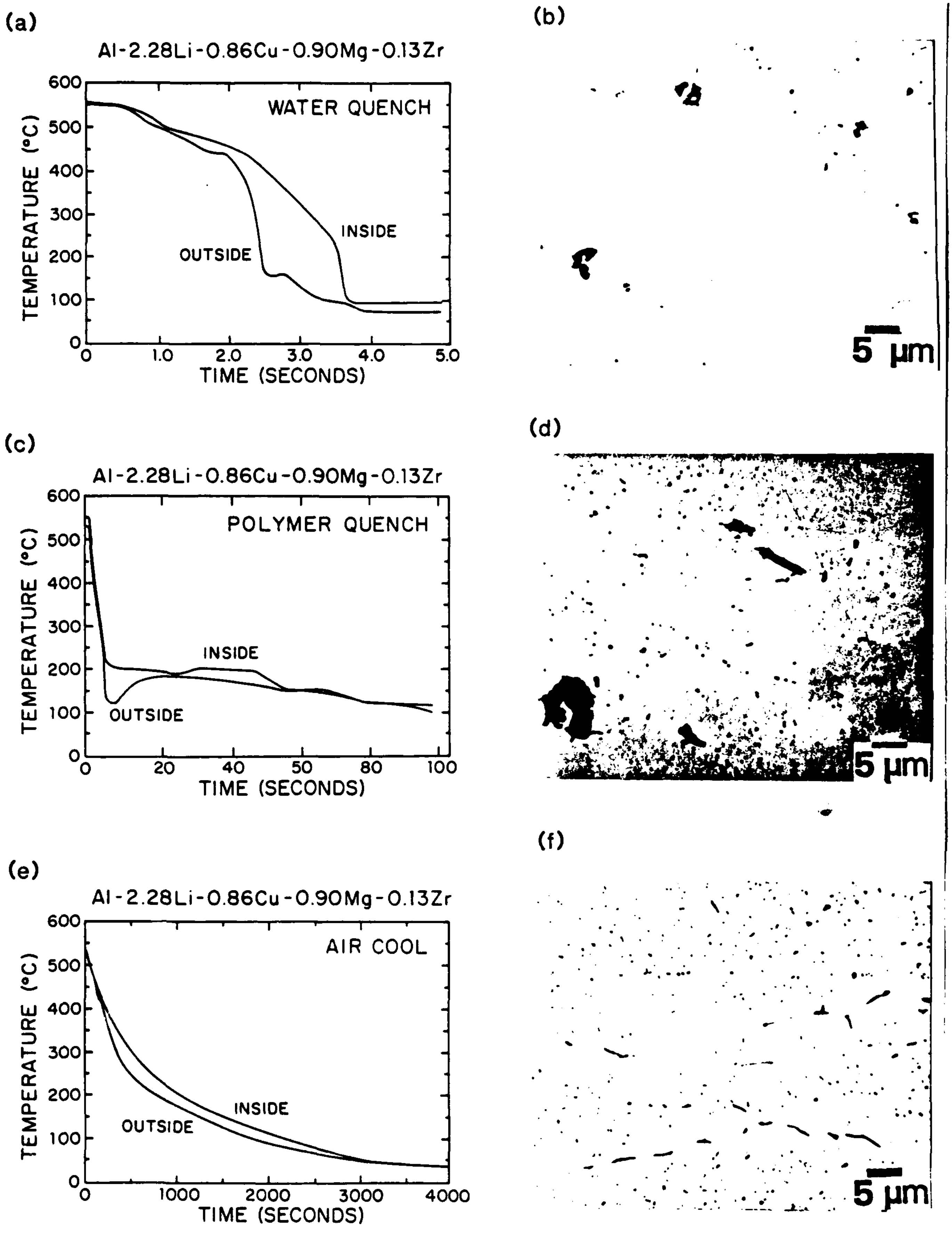

Figure 1. Cooling curves and associated RT microstructures for the lean 8090 alloy. (a-b) 150°C/sec; (c-d) 9°C/sec; (e-f) 0.2°C/sec.

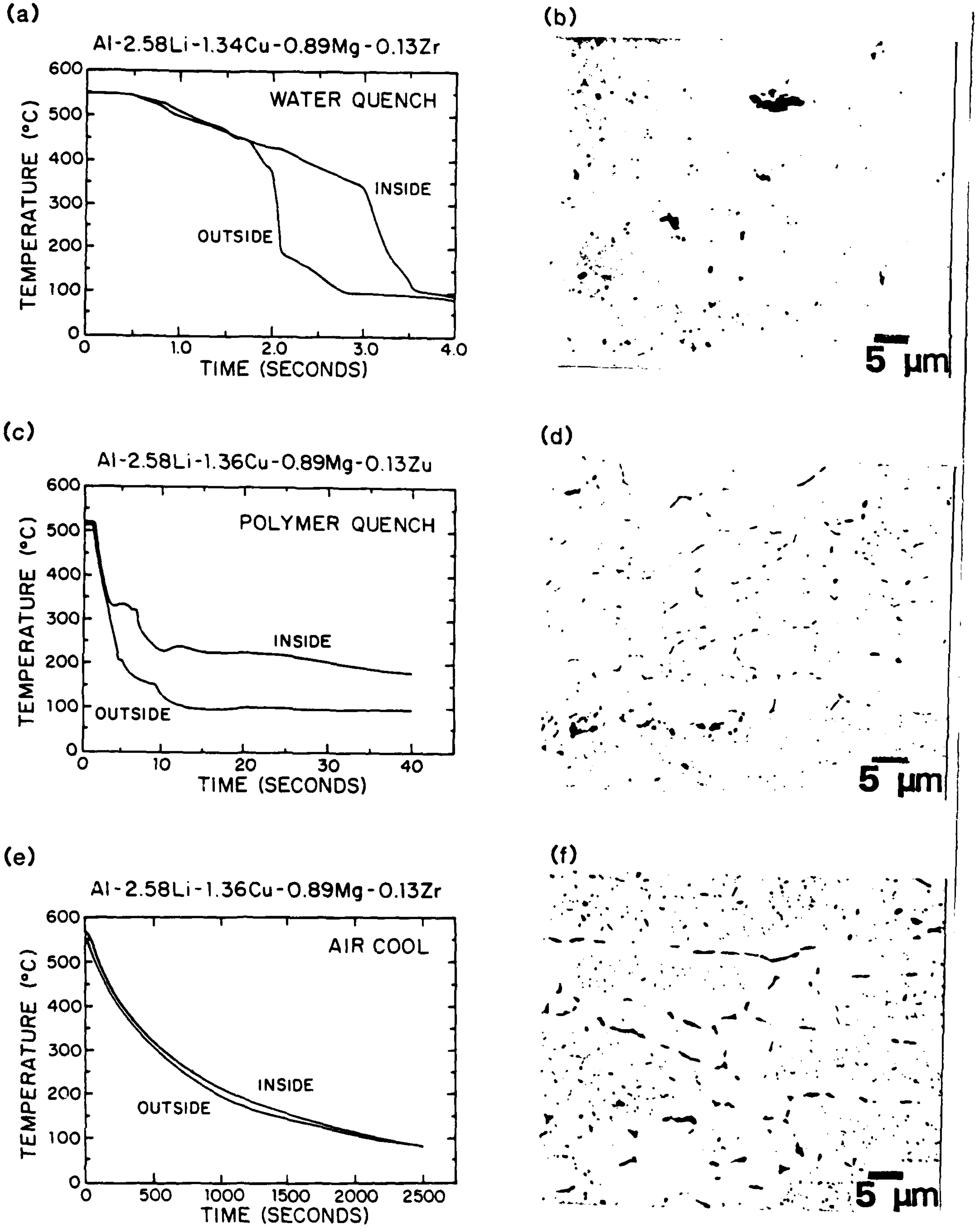

Figure 2. Cooling curves and associated RT microstructures for the rich 8090 alloy. (a-b) 150°C/sec; (c-d) 9°C/sec; (e-f) 0.2°C/sec.

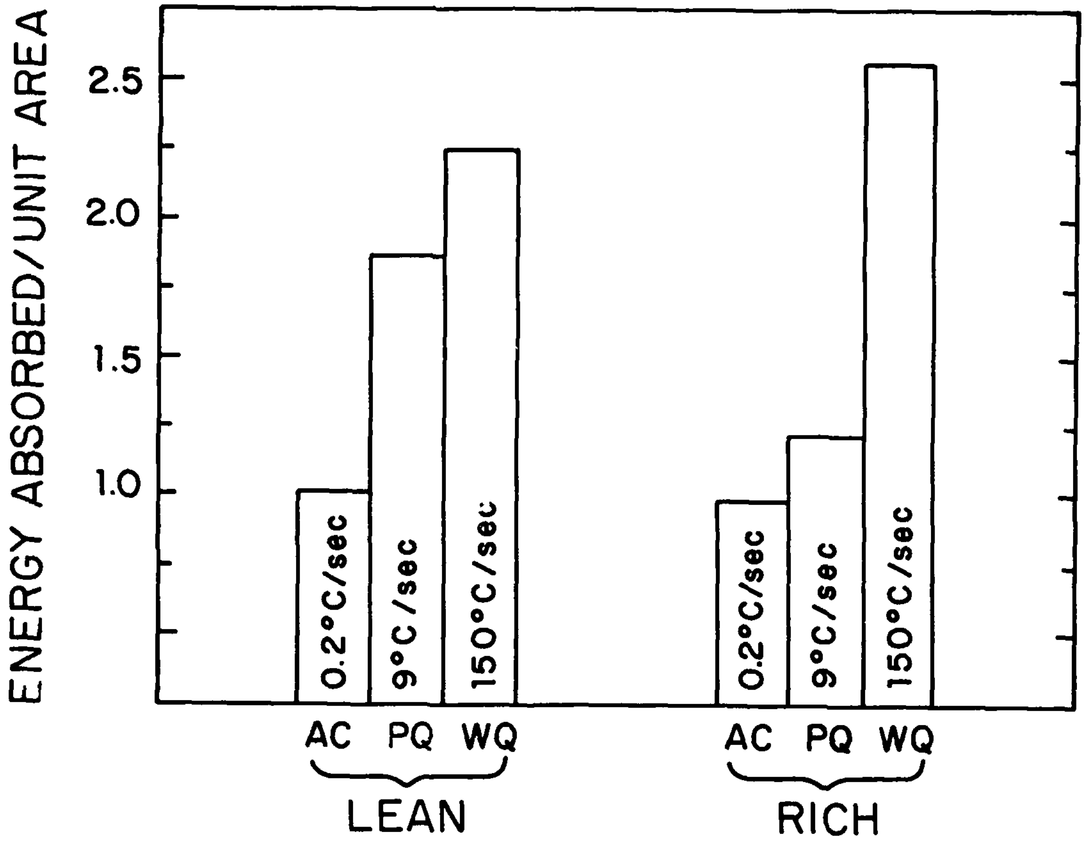

Figure 3. Normalized Charpy energy absorption values showing drop in fracture resistance with decreasing quench rates.

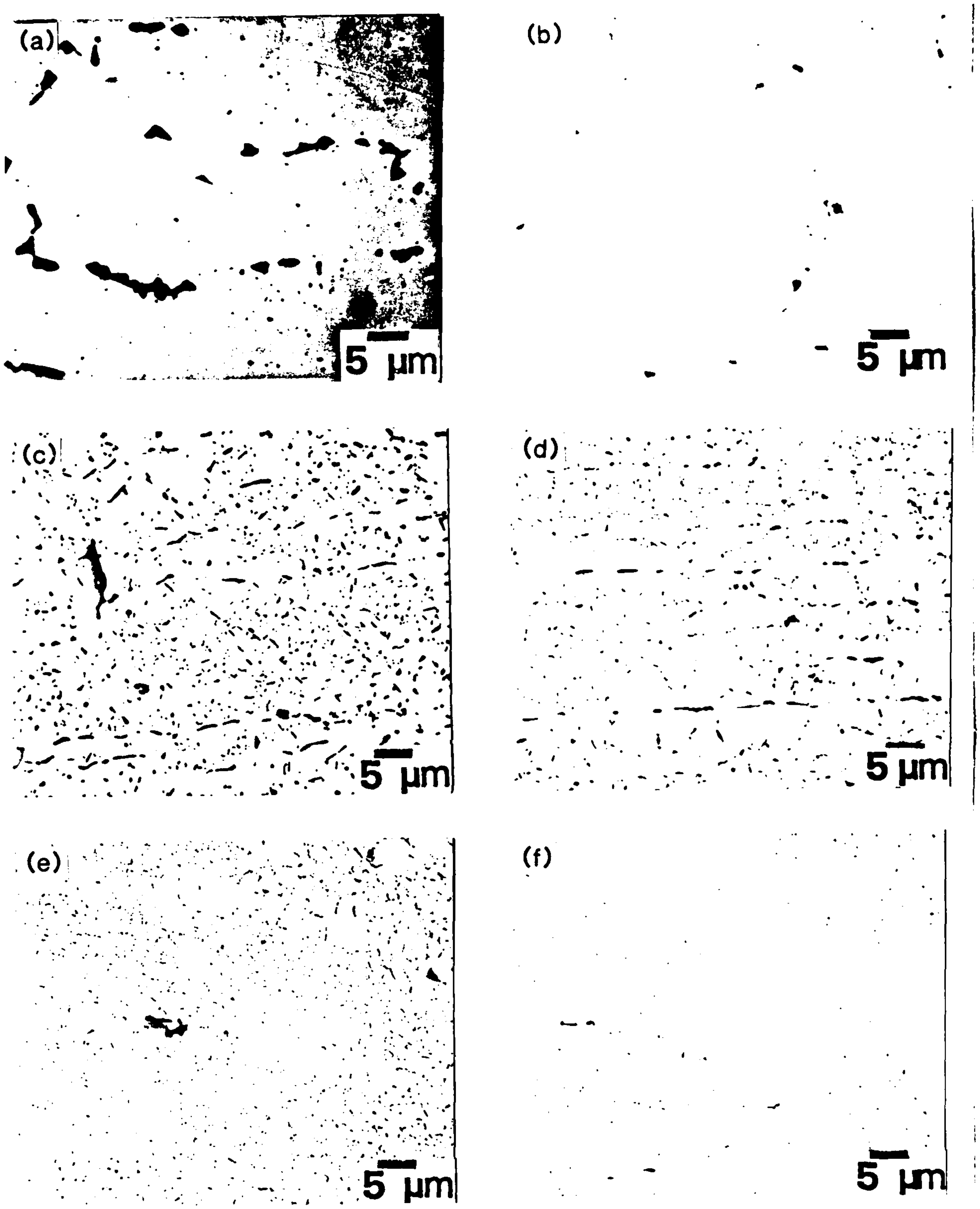
(a)
5 µm
(b)
5 µm
(c)
5 µm
(d)
5 µm
(e)
5 µm
(f)
5 µm

Figure 4. Optical micrographs of the rich and lean 8090 alloys after 1000 sec at various temperatures; a, c, e, rich alloy at 500°, 400° and 300°C, and b, d, f, lean alloy at 500°, 400° and 300°C, respectively.

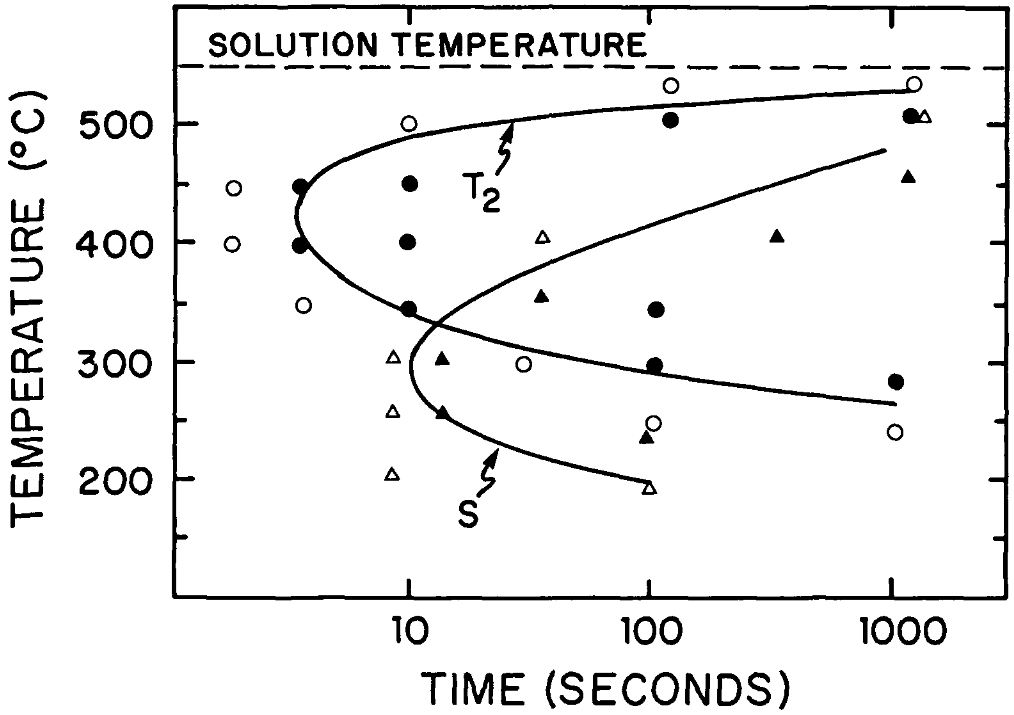

Figure 5. Nucleation start curves for T_2 (Al_6CuLi_3) and S (Al_2CuMg) for the rich 8090 alloy.

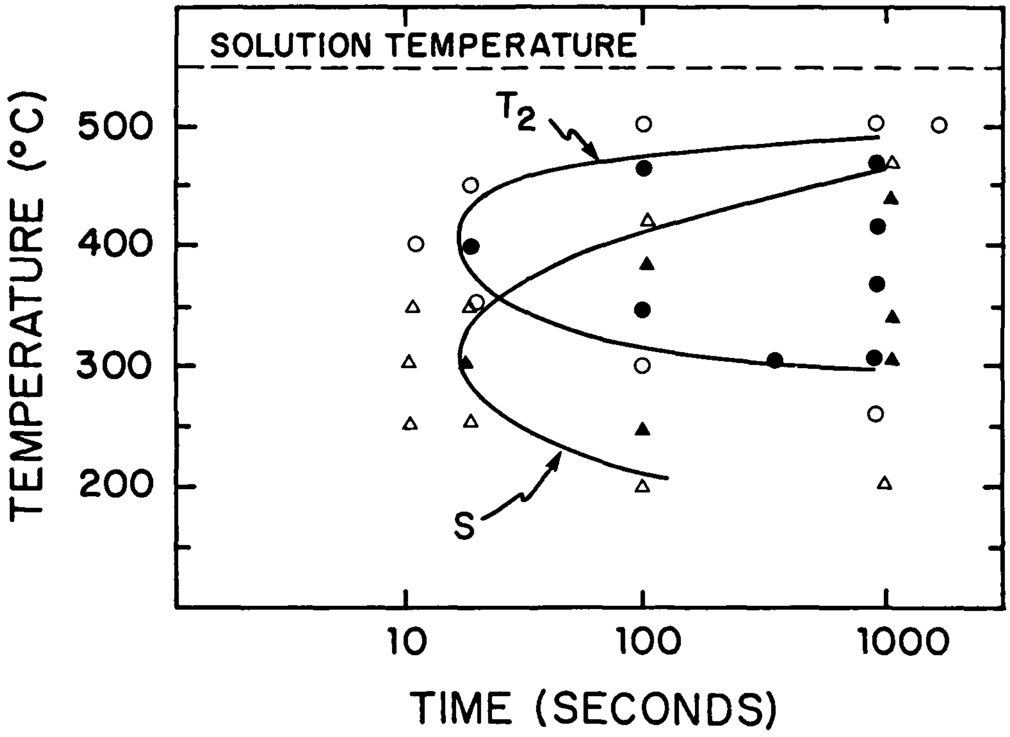

Figure 6. Nucleation start curves for T_2 (Al_6CuLi_3) and S (Al_2CuMg) for the lean 8090 alloy.

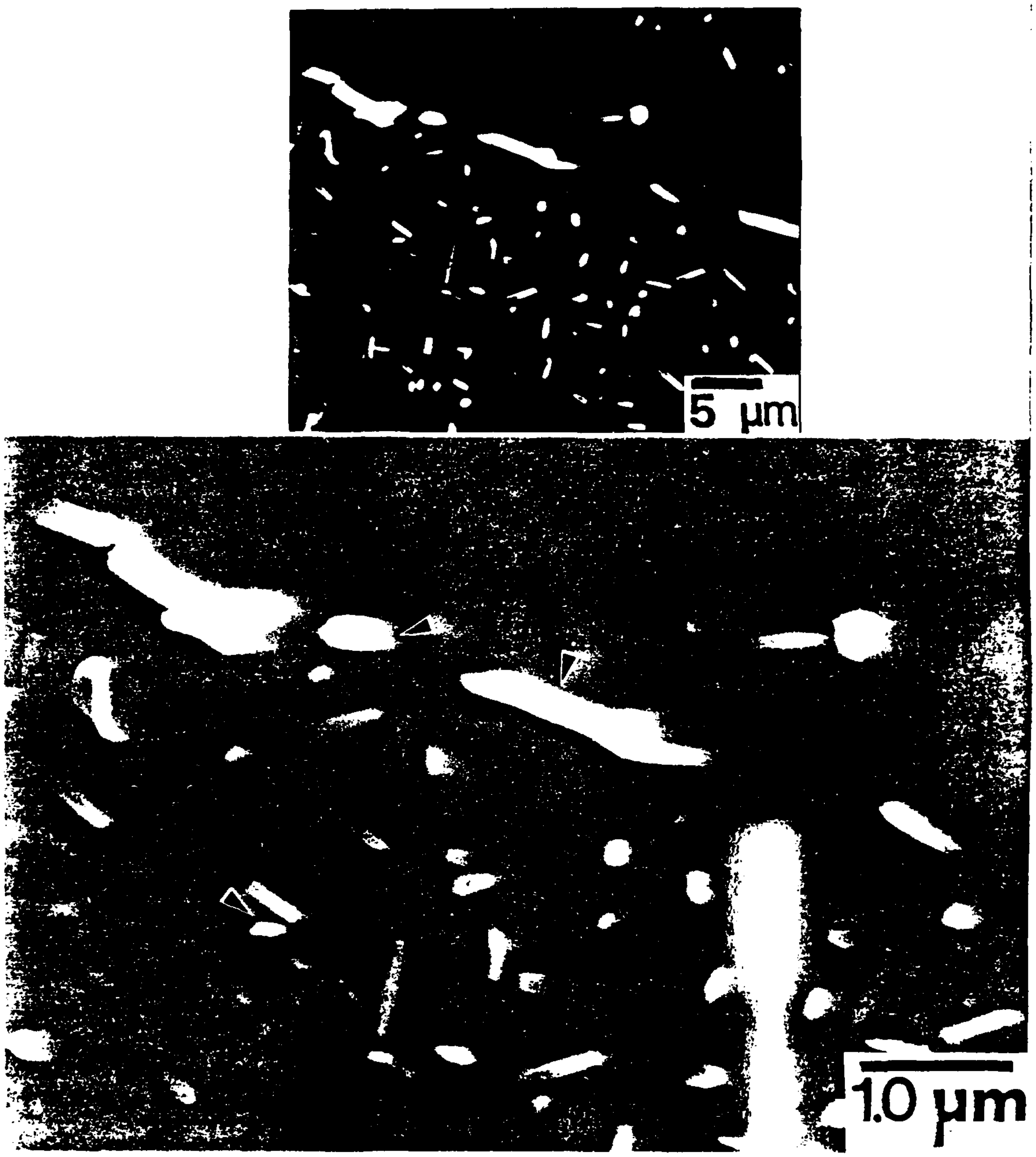

Figure 7. SEM of the 8090 alloy after etching with boiling 1:9 Bromine:Methanol solution showing the T_2 and S precipitates.

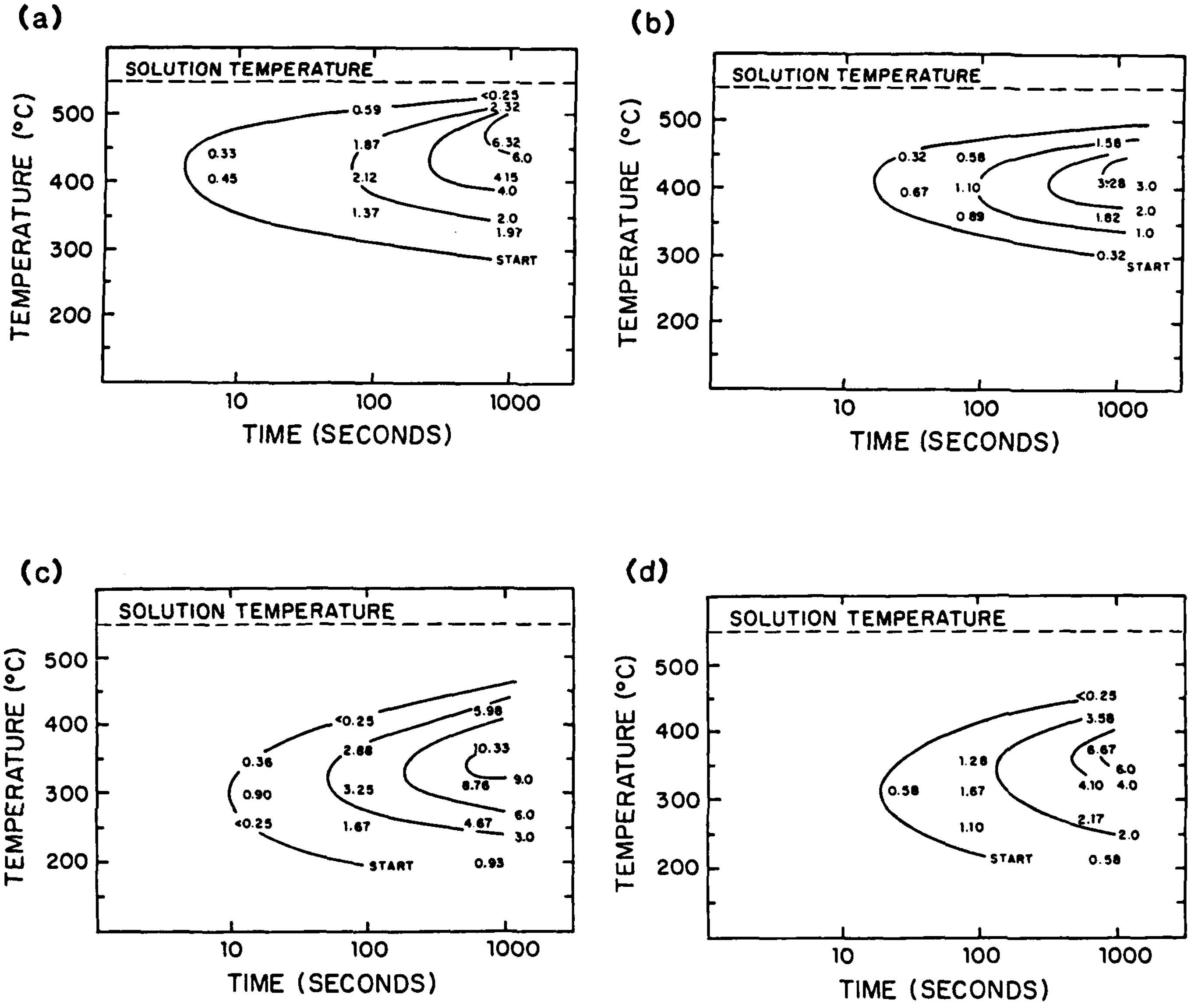

Figure 8. Time-temperature-transformation curves showing volume percents of the T_2 and S phases. (a) T_2 for the rich alloy; (b) T_2 for the lean alloy; (c) S for the rich alloy and (d) S for the lean alloy.

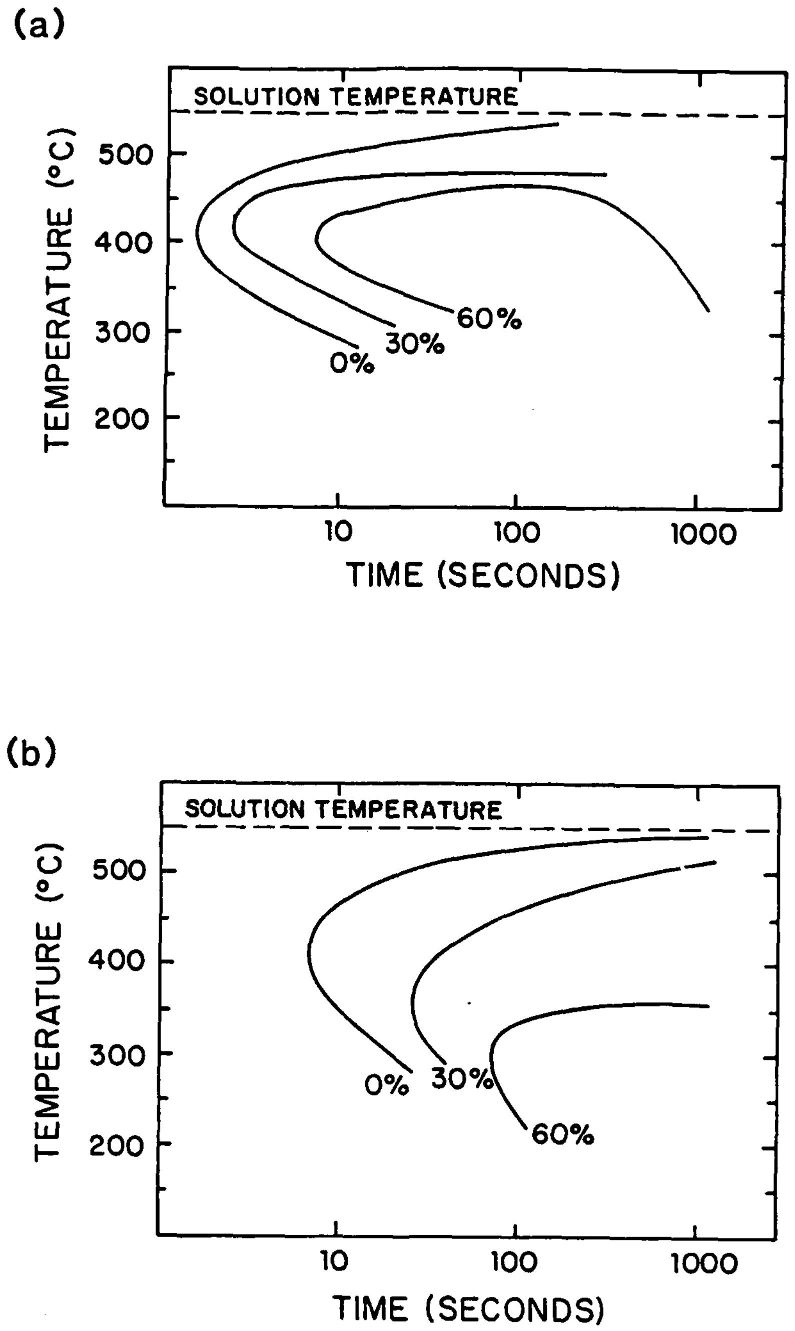

Figure 9. Iso mechanical lines showing the percent loss of Charpy energy values as a function of time at various temperatures, (a) rich 8090 alloy and (b) lean 8090 alloy.

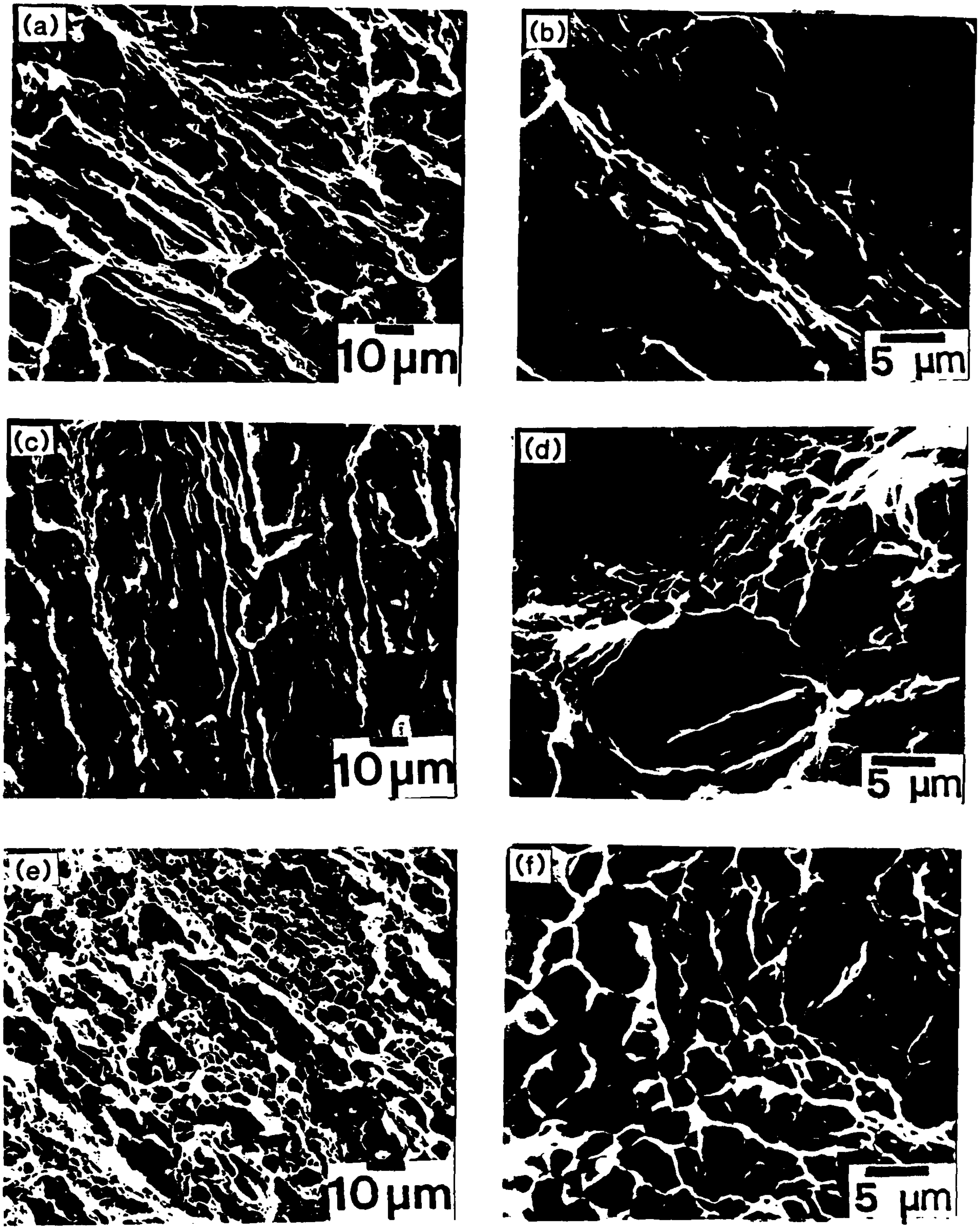
(a)
10 μm
(b)
5 μm
(c)
10 μm
(d)
5 μm
(e)
10 μm
(f)
5 μm

Figure 10. Representative SEM's of fracture surfaces of the rich and lean alloys after various times at 400°C. (a-b) 10 secs, (c-d) 100 sec, and (e-f) 1000 sec.

PART II. PROCESSING OF ADVANCED ALUMINUM ALLOYS FOR STRUCTURE CONTROL

J.A. Wert, H. Gudmundsson and D. Brooks

ABSTRACT

Reduction of grain size in aluminum alloys can increase strength and can lead to superplasticity during elevated temperature deformation. Thermomechanical processing for grain size control relies on particle dispersions to manage relaxation (recovery and recrystallization) of the deformation substructure. This study has focused on the recovery and recrystallization mechanisms in a model alloy with composition Al-0.24Zr-0.1Si. This alloy contains a high density of dispersoid particles which provide a drag pressure on migrating boundaries sufficient to retard discontinuous recrystallization. The distribution of dispersoid particles, the deformation microstructure after cold rolling and the annealing conditions were found to be important variables affecting the recovery and recrystallization kinetics of the alloy. The results indicate how the microstructure evolves during static annealing and during concurrent annealing and elevated temperature deformation.

1. INTRODUCTION

The purpose of this study is to identify the mechanisms of evolution of subgrain and grain structures in aluminum alloys that contain a high density of dispersoid particles, and to establish the material and processing parameters that control microstructure evolution. This introductory section describes some basic features of the recovery and recrystallization mechanisms that contribute to microstructure evolution, and show what aspects of these processes are incompletely understood.

Conventional recrystallization proceeds by nucleation of new grains in a deformation substructure and growth of these grains until impingement. Recrystallization fronts that sweep through the deformed microstructure are high-angle boundaries, which have much higher migration rates than low angle boundaries (1). Since passage of a high-angle boundary leads to an abrupt, or discontinuous, change in defect density and lattice orientation, the term discontinuous recrystallization has been used to describe this process.

Recovery is an alternate path for relaxation of the stored energy of deformation; one which does not proceed by nucleation and growth of new grains. Instead, recovery occurs by the gradual processes of polygonization, subgrain growth and subgrain coalescence. Recovery is a continuous process since it occurs gradually throughout the deformation microstructure. Ordinarily, however, recovery does not produce high-angle grain boundaries. There are two reasons for this. First, misorientations between adjacent dislocation cells or microbands in the deformation microstructure are mostly small and migration of low-angle boundaries over short distances cannot increase the misorientation appreciably. Second, the more rapid process of discontinuous recrystallization often obliterates the recovering substructure before recovery has proceeded very far. Since recovery produces predominately low-angle boundaries, microstructures produced by recovery are not suitable for superplastic deformation.

A limited number of observations indicate that if discontinuous recrystallization does not intervene, recovery continues by subgrain boundary migration (and possibly subgrain coalescence), eventually producing a grain structure that contains moderate-to-high angle boundaries and a small grain size. The resulting microstructure resembles a discontinuously-recrystallized microstructure, but the process is not a classical recrystallization process because high-angle boundary migration is not required. This process has been termed "extended recovery" or "continuous recrystallization".

Two factors are thought to be needed to extended recovery to occur. First, the much more rapid discontinuous recrystallization process must be suppressed. The only method known to accomplish this is introducing particle dispersions which provide drag pressures sufficient to prevent nucleation of discontinuous recrystallization, and yet allow slow migration of subgrain boundaries. Solute atoms in solid solution may also contribute to the boundary drag pressure in some cases. Second, recovery processes must be accelerated. The only method known by which this can be done is concurrently annealing and deforming a material. If both of these conditions are met, recovery processes eventually lead to formation of medium to high-angle boundaries (>10° misorientation) without requiring high angle boundary migration (2,3). While discontinuous recrystallization leads to a change in texture, the rolling texture is retained during extended recovery, although its strength usually decreases (2,4). The best-known examples of extended recovery in aluminum are alloys containing high densities of Al_3Zr dispersoids, or in powder metallurgy alloys containing high densities of oxide particles (5,6).

Extended recovery is the method used to develop superplastic characteristics in a wide variety of aluminum alloys. SUPRAL^{TM} (Al-Cu-Zr), the most widely-used commercial superplastic aluminum alloy, employs Al_3Zr and Al_2Cu particles to suppress discontinuous recrystallization, thus allowing extended recovery an opportunity to generate a microstructure suitable for superplastic forming. A wide variety of new aluminum alloys; including various Al-Li alloys, mechanically-alloyed aluminum alloys, and aluminum alloy composites; can be made superplastic by thermomechanical processing treatments that employ extended recovery to produce a fine grain microstructure. Thus, processing of alloys that undergo extended recovery is currently of technological and economic importance, and this processing method seems likely to become more important as demand increases for newer aluminum-base materials to be fabricated into useful components.

Despite the utility of the extended recovery processing method, several basic questions remain unanswered.

1. Does concurrent annealing and deformation introduce new mechanisms of microstructure relaxation that are not available by annealing alone?
2. What features of the deformation microstructure play key roles in the extended recovery process?
3. By what mechanism does the elevated temperature deformation speed-up recovery?

The ultimate goal of this research project is formulation of a model that will enable processing parameters for extended recovery to be selected and optimized for a wide variety of aluminum alloys. Answers to the basic questions listed above are needed before such a model can be formulated. The present investigation has focused on an Al-Zr-Si alloy as a model material which exhibits all of the relaxation phenomena being studied without superposition of complicating effects such as precipitation.

2. EXPERIMENTAL PROCEDURE

2.1 Materials and Material Preparation

The alloy investigated in this study was an Al-Zr-Si alloy with analyzed composition: 0.24 wt% Zr, 0.1 wt% Si, 0.01 wt% Fe, 0.02 wt% Ni and 0.03 wt% Zn. The Al-Zr-Si alloy was provided by Reynolds Metals in the form of a direct-chill-cast ingot (dimensions 25 cm x 16 cm x 6.5 cm). A mechanically-alloyed Al-O-C alloy provided by INCO Alloys International has also been investigated; results pertaining to this alloy will be included in a future report.

In binary Al-Zr alloys, small coherent Al_3Zr particles can be made to precipitate from a solid solution but the reaction is slow and the resulting particle distribution is uneven (7). Because of the low solubility of Zr in aluminum (0.28wt.%) and because the binary system is a peritectic (8), it is necessary to chill the melt quickly to retain a high supersaturation of Zr and to prevent formation of coarse Al_3Zr primary particles. Small additions (0.1 wt.%) of Si have been reported (9) to accelerate the precipitation and homogenize the distribution of Al_3Zr particles when the heating rate to the annealing temperature is slow ($< 50^{o}C/hr$). After precipitation, the Al_3Zr particles coarsen very slowly for annealing temperatures less than $440^{o}C$ (10).

Specimens (dimensions 11 mm x 15.5 mm x 56 mm) were cut from the Al-Zr-Si ingot and heat-treated to precipitate Al_3Zr particles. The specimens were cut from the edges of the ingot and annealed in air for 8 hrs at $450^{o}C$ with a $50^{o}C/hr$ heating rate to the annealing temperature. Cold rolling of the Al-Zr-Si specimens was done in 10% increments of reduction to a total of 60 - 90% reduction in thickness (effective strains of 0.9 to 2.5). After each rolling pass the specimen was cooled with water to limit recovery and the specimens were stored in a freezer to minimize recovery after rolling. The microstructure of the cold-rolled specimens was analyzed and the Vickers hardness was measured prior to annealing for recovery and recrystallization.

2.2 Microstructural Characterization

Characterization of the microstructures was performed using optical microscopy, transmission electron microscopy (TEM), scanning electron microscopy (SEM) and X-ray texture measurements. Cross-sections normal to the longitudinal and long transverse directions were mounted in epoxy and polished using conventional methods. The as-polished specimens were normally anodized (20 V, 1 min) using Barkers etch at room temperature. A few samples were etched in a 1:10 NaOH - H_2O solution at 65^oC for 3 minutes.

Cross-sections normal to the transverse direction were cut with a diamond blade using a low-speed saw and carefully ground with 600 grit paper to a thickness of 150 μm. Depending on the short-transverse thickness of the plates, TEM specimens (3 mm disks or 3 mm strips) were either punched-out or cut from the cross-sections. The TEM specimens were electropolished in a 1:3 nitric acid - methyl alcohol solution at -25^oC using a double jet apparatus.

X-ray texture measurements were performed with a Siemens texture diffractometer using Cu K_α radiation. Texture specimens were carefully ground and polished to a 1 μm surface finish and then they were electropolished (15V, 2 min) in a 1:3 Nitric acid - Methyl alcohol solution at -45^oC.

2.3 Concurrent Annealing and Deformation

Tensile specimens were machined from sheets of the Al-0.24Zr-0.1Si alloy which had been cold rolled to a strain of 2.5 (effective strain). Prior to testing, the tensile specimens were ground and polished to a 1 μm surface finish. Reference lines were scribed lightly on the gauge section in case the strain would have to be measured from the sample itself. For accurate temperature measurements during tensile testing, a thermocouple wire was attached to the gauge section with a thin copper wire.

The elevated temperature testing was done at constant crosshead velocity using an Instron machine equipped with a three-zone furnace. The experimental setup allowed quick removal of the tensile specimens and water quenching after straining. Load vs time (extension) data were sampled by a computer connected to the load cell. From the data, stress vs strain curves were calculated.

The Al-Zr-Si tensile specimens were strained to failure at 400°C for crosshead velocities between 0.05 and 5 cm/min, corresponding to initial strain rates between 6.5×10^{-4} s^{-1} and 6.5×10^{-2} s^{-1}. The specimens reached the testing temperature in about 1 hour and were stabilized at that temperature for 20 minutes prior to testing. Based on the results of these first tests, further tensile testing was done using the same temperature and the slowest strain rate (6.5×10^{-4} s^{-1}). These tests were stopped at lower strain values to determine the effect of strain on microstructure evolution. The tensile specimens were stored in a freezer after testing to minimize room temperature recovery. Cross-sections from the grip and gauge section of each of the tensile specimens were prepared for metallography. Selected cross-sections were prepared for TEM analysis.

3. RESULTS

3.1 Microstructure of the Al-0.24Zr-0.1Si Alloy

Polished cross-sections of the specimens chosen for heat treatment exhibited a coarse grain size (grain diameter 1 - 2 mm) which remained constant during the heat treatment. No Al_3Zr primary particles could be seen in the metallographic sections. After heat treatment, small coherent Al_3Zr precipitates were observed in the specimens by TEM. The particle radius was measured on dark-field micrographs for about 300 particles. The average particle radius was calculated to be (4.7 ± 0.5) nm. Using the Zener relation for drag pressure, the average particle drag pressure in the alloy is:

$$P_Z = 2\beta\gamma(f/r) = (0.37 \pm .04) \text{ MPa}$$

In this calculation, a value of 0.3 J/m^2 was used for the boundary energy (11), a value of 1 was assumed for β (12), and all of the Zr was assumed to be precipitated in the form of Al_3Zr particles.

TEM observations showed the Al_3Zr particle distribution to be uneven. By etching a heat-treated cross-section (1:10 NaOH/H_2O, 2 minutes at 65^oC) from the edge of the casting, a dendritic structure appeared (Fig. 1). Qualitative Energy Dispersive X-ray Spectroscopy (EDS) revealed that the light dendrites in the figure contain more Zr and Si than the darker areas in between. In this alloy, the Zr tends to segregate to areas that solidify first, while the Si should segregate to areas that solidify last.

3.2 Deformation Microstructure of Al-0.24Zr-0.1Si

The Zr-enriched dendrites have a great effect on the deformation and annealing behavior of the alloy. Figure 2 shows optical micrographs of polished and anodized cross-sections after various rolling strains. The micrographs show how the dendrites act as hard "islands" in the matrix and how the deformation substructure flows around them. With increasing rolling reductions, the dendrites become more flat and the spacing between them decreases. Figure 3 shows a part of a hard dendrite after rolling to a 75% reduction in thickness (strain = 1.5). The high density of Al_3Zr particles delays the formation of deformation cells in the dendrite and influences the flow of material outside it. The deformation cells around the dendrite contain a lower density of particles.

After a 90% reduction in thickness (strain = 2.5) there is still a difference in the deformation structure for areas that have different particle densities. TEM observations show that narrow microbands characterize areas of lower particle density, whereas in areas where the particle densities are high, the deformation structure is not well defined.

Transverse orientations for selected groups of microbands were obtained from convergent beam diffraction patterns and are shown in Figure 4. Each circle corresponds to the orientation of a single microband and the figure shows that most of the microbands have a {110} plane approximately parallel to the transverse direction (T). Misorientations between adjacent microbands were determined by measurement from a Wulff net or calculated from the electron beam orientations obtained from the convergent beam diffraction patterns.

The maximum error in the misorientation value is estimated to be $\pm 0.5^\circ$. Most of the misorientations for the data in Figure 4 is in the range of $0.8^\circ - 5^\circ$. However, a region shown in

Figure 5 was found to have higher misorientations between microbands. The nature of this particular region cannot be determined from this data alone, but it may be that the hard dendrites produce high local misorientations in the adjacent deformed material.

3.3 Relaxation of Cold-Rolled Al-0.24Zr-0.1Si

As was shown in the last section, rolling to larger strains leads to a more homogeneous deformation microstructure. The microstructural homogeneity was reflected in the mode of relaxation during subsequent annealing. Preliminary studies suggested that rolling to a strain of 2.5 made the alloy more resistant to discontinuous recrystallization by making the particle distribution and deformation microstructure more homogeneous. This rolling strain was therefore chosen for further studies on the effect of annealing variables.

3.3.1 Effect of Annealing Temperature on Relaxation of Cold-Rolled Al-0.24Zr-0.1Si

Figure 6 shows the hardness as a function of annealing temperature for Al-0.24Zr-0.1Si rolled to a strain of 2.5. The drop in hardness for annealing temperatures greater than 350°C is due to increasing discontinuous recrystallization in the deformation microstructure. At the higher annealing temperatures, more nucleation and growth of recrystallized grains takes place before recovery can lower the driving pressure. The combined effect of recovery and boundary drag pressure may halt the growth of a nucleated grain at a later stage. However, if the driving pressure on the migrating boundaries is high enough, the deformation microstructure will become fully recrystallized.

In a specimen annealed for 8 hours at 400°C, the volume fraction recrystallized was determined by quantitative metallography to be (34 ± 7)%. However, for the same specimen, the hardness drop was approximately 64% so it was apparent that considerable recovery had also taken place in the unrecrystallized portions of the deformation microstructure. Indeed, TEM observations of this specimen revealed a well-recovered but nonuniform microstructure.

Annealing at 450°C led to an almost fully recrystallized microstructure with an average grain size of (50 ± 5) μm. The hardness value was determined to be (277 ± 11) kgf/mm^2, which is a slightly lower value than that measured for the as-heat-treated material, (296 ± 15) kgf/mm^2, but the difference is not statistically significant. If the hardness is in fact lower after recrystallization it could be due to dissolution of Al_3Zr particles by migrating high angle boundaries. This phenomenon was observed in this study and will be discussed in a later section.

3.3.2 Effect of Isothermal Annealing on the Relaxation of Cold-Rolled Al-0.24Zr-0.1Si

The next step was to determine whether annealing temperatures lower than 400°C would lead to a more continuous evolution of the deformation microstructure.

Figure 7 shows the hardness as a function of annealing time for three different temperatures: 350°C, 375°C and 400°C. The sharp initial drop in hardness during annealing at 400°C is due to recovery and discontinuous recrystallization which takes place during the first few minutes at the annealing temperature. Figure 8A shows discontinuous recrystallization after 15 minutes at 400°C. The elongated shape of the grains suggests that the growth is less retarded in the rolling plane. The shape of the grains is consistent with the idea that they nucleate between the elongated dendrites observed in the deformation microstructure. After a period of 48 hours at 400°C, the hardness value had dropped to (290 ± 8) kgf/mm^2 and metallography examination showed an almost fully recrystallized microstructure with grains of various diameters (Fig. 8B).

The hardness evolution at 375°C shows a similar initial drop but after about 1 hour the hardness decrease becomes very gradual. The initial drop in hardness can, in this case, also be attributed to both recovery and discontinuous recrystallization during the first few minutes of annealing. Figure 8C shows recrystallized grains after 48 hours at 375°C. The largest grains probably nucleated during the early part of the annealing but their growth slowed down or halted after that.

The hardness evolution during annealing at 350°C is more gradual due to slower recovery kinetics and less discontinuous recrystallization. After 72 hours at 350°C the microstructure looks well-recovered with almost no large grains (Fig. 8D). With decreasing annealing temperature both recovery and recrystallization kinetics become slower, but the high particle drag pressure can delay or prevent nucleation of recrystallized grains, thus making the conditions more favorable for extended recovery.

3.4 Evolution of Texture During Annealing

Texture measurements were done on specimens annealed at 350°C and 375°C to study the texture evolution during annealing. Figure 9 shows a partial (111) pole figure for an annealed specimen (350°C ,72 hours) and the (111) pole figure for the as-rolled specimen for comparison. The texture of the annealed specimen is somewhat weaker, but it is still similar to the rolling texture. This indicates that mostly recovery has taken place, i.e. the orientations in the deformation microstructure have not changed appreciably.

During annealing at 375°C the texture becomes weaker and more random. Figure 10 shows the (111) pole figures of specimens annealed for 24 hrs and 48 hrs. After 24 hours of annealing the rolling texture is still retained, but after 48 hours of annealing the texture is more random. After 24 hours at 375°C the volume fraction recrystallized is (17 ± 9)% and the volume fraction increased to (30 ± 10)% after 48 hours at 375°C. It is apparent that orientations in the deformation microstructure have changed although the microstructure is still not fully recrystallized (Fig. 8C).

3.5 Quantitative Evaluation of Microstructure Evolution During Annealing

The results of the previous sections have shown that discontinuous recrystallization occurs faster at high annealing temperatures. For a subgrain to become a recrystallization nucleus, it must be surrounded in part by a highly mobile interface (13). Studies of deformed specimens after long and short annealing times at lower temperatures show that the microstructural evolution is influenced by the particle distribution and high angle boundaries formed in the deformation microstructure.

Figure 11 shows a region from the microstructure of a sample annealed for 8 hours at 350°C. This region is undergoing polygonization, i.e. the microbands are evolving to a subgrain structure (14). The microbands are in a region with a higher density of Al_3Zr particles and show slower evolution. The misorientations between subgrains were determined from convergent beam diffraction patterns. Some examples of misorientations are shown in Figure 11. A striking feature of these results is the wide range of boundary misorientations across the microbands (approximately 2 - 19°), in contrast to smaller misorientations along the microbands (0.8 - 4°). The boundary misorientations in this area are favorable for subgrain coalescence in the direction of the microbands. That way the low-angle boundaries disappear while the high-angle boundaries increase their misorientation slightly. This mechanism may already be in progress in the specimen shown in Figure 11. A pole figure generated from the transverse orientations in this area is shown in Figure 12 along with the orientations of the subgrains. A pole figure supplements the information given by the misorientation value by better illustrating the orientation relationship between subgrains and grains.

Figure 13 shows two well-recovered regions in the microstructure of a specimen annealed at 350°C for 72 hours. Some of the subgrains in the figure are almost free of the small Al_3Zr particles, while some larger incoherent Al_3Zr particles lie on or close-to boundaries. Apparently some of the boundaries have dissolved small Al_3Zr particles during migration, leading to subsequent precipitation of large, incoherent Al_3Zr particles. Qualitative EDS analysis of the large particles shows the presence of Zr and identical observations made by other workers (15,16) support this argument. Some examples of boundary pinning by particles can be seen in Figure 13. Other regions in the microstructure are not as well recovered or still show deformation microstructure features such as microbands. A high particle density characterizes these areas of retarded recovery (upper corner of Figure 13B).

Misorientations between subgrains were studied in this specimen and some examples are shown in Figure 14. The first region shows well-developed subgrains separated by low-angle boundaries. The second region contains high-angle boundaries approximately parallel to the rolling direction. The largest subgrains in this area are surrounded in part by high angle boundaries pinned by particles.

The orientations of the subgrains in these two areas lie on a large circle between the [101] and the [123] directions (Figure 14). These orientations are generally seen in deformation microstructures of cold worked fcc metals and alloys. The (111) pole figure for these orientations shows more texture components than the pole figure for the 8 hour anneal. However, the misorientations observed after a 72 hour anneal are not much greater than those observed after an 8 hour anneal.

Annealing at 375°C lead to a more random X-ray texture after a 48 hour anneal although the volume fraction recrystallized was low (about 30%). Figure 15 shows an area of the microstructure after a 48 hour anneal. Again, most of the high angle boundaries are parallel to the rolling direction and most of the low angle boundaries are transverse to the rolling direction. The boundaries are pinned by coarse Al_3Zr particles. The subgrain orientations in one of these areas are shown in Figure 16A. The labeled orientations are from the region shown in Figure 15 and other regions. Most of the orientations are not typically seen in cold worked fcc metals and corresponding pole figure (Figure 16B) does not show a definite texture for these two regions.

3.6 Concurrent Annealing and Deformation of Al-0.24Zr-0.1Si

3.6.1 Effect of Concurrent Annealing and Deformation on the Flow Stress

The true stress - true strain curves for tensile specimens tested for three different strain rates at 400°C are shown in Figure 17. The values for the true stress and strain were calculated from the load vs extension data. The samples were strained to failure to determine the maximum elongation and the strain-rate sensitivity. The stress - strain curves show a decrease of flow stress after a maximum at a strain of approximately 0.1. This decrease in flow stress is due to both softening of the material and necking of the gauge section during deformation.

The strain to failure decreases from about 0.76 to 0.33 as the strain rate increases from 6.5×10^{-4} s^{-1} to 6.5×10^{-2} s^{-1}. The strain rate sensitivity, m, was calculated to be 0.2 for the strain rate range studied.

Two more tensile specimens were deformed to strains of 0.22 and 0.46 at the slowest strain rate. After testing, the cross-sectional area of the gauge sections were measured to determine the actual flow stress at the end of the test. For the specimen tested to a strain of 0.22 it was found that $(A_o/A) = (L/L_o)$, therefore no correction to the flow stress was necessary. For the specimen tested to a strain of 0.46 it was found that $(A_o/A) = 1.1 \times (L/L_o)$. The flow stress at that strain is therefore a factor 1.1 too low. However, even with this correction the flow stress at a strain of 0.46 is lower than the peak stress. The shape of the curve is then correct at least up to a strain of 0.46, indicating that softening is taking place during deformation.

3.6.2 Effect of Strain on Microstructural Evolution During Concurrent Annealing and Deformation

Of the three strain rates that were used, only the slowest strain rate enabled the substructure in the deformed sections of the tensile specimens to relax fully. Cross-sections from tensile specimens tested to various strains were studied using optical microscopy and TEM.

Studies of cross-sections normal to the transverse direction show that the substructure in the gauge section appears to be fully relaxed after a strain of 0.46, while the undeformed grip sections show a slightly recovered microstructure with some discontinuously recrystallized grains. Figures 18 and 19 show polished and anodized cross-sections from a grip section and deformed gauge sections tested to a strain of 0.22, 0.46 and 0.76.

All of the gauge sections show some discontinuous recrystallization. The results described in Section 3.5 and the observations of microstructure of the grip section suggest that the discontinuous recrystallization takes place during the heating to test temperature. However, the specimen tested to a strain of 0.76 contains the largest discontinuously-recrystallized grains.

Figure 20 shows an area from the deformed section after a strain of 0.22. Since the specimen was quenched in the grips at the same time the straining was stopped, numerous dislocations can be seen inside the subgrains. Both fine and coarse Al_3Zr particles are present and interfere with the movement of dislocations and boundaries. Observation of dislocations indicate that a dislocation creep mechanism is responsible for at least some of the strain. Most of the high angle boundaries lie parallel to the tensile direction/rolling direction and examples of boundary coalescence can be seen in the first area. The orientations seen in this field and others are plotted on the pole figure shown in Figure 21. The orientations and the resulting texture are similar to that seen during the initial stages of static recovery.

The deformed section of specimens tested to a strain of 0.46 and 0.76 contain both large (>100 μm) elongated grains and small, slightly elongated grains. While the size of the larger grains increases somewhat with increasing strain, the increase in grain size of the smallest grains is not statistically significant. For a strain of 0.46, the average size of the smallest grains is

(8.8 ± 1.5) μm, for a strain of 0.76 the size of the smallest grains is (11 ± 1.8) μm.

The microstructure of an undeformed grip section (from the specimen tested to a strain of 0.22) shows low- to medium-angle boundaries oriented parallel to the tensile direction (Figure 22). The microstructure in the grip section is undergoing recovery while the deformed gauge section is fully relaxed.

4. DISCUSSION

4.1 Deformation Microstructure of Al-Zr-Si

In Section 3.2 it was shown how the distribution of Al_3Zr particles in the Al-0.24Zr-0.1Si alloy affects formation of the deformation substructure as a function of rolling strain. While the Zr-rich dendrites are initially harder than the matrix, the plastic strain is concentrated in the matrix around them. As the matrix around the dendrites work hardens, the dendrites will gradually deform more. At the same time, the rolling process is squeezing the dendrites together. Figure 3 shows how areas of high particle density gradually change their appearance as the rolling strain increases from 1.5 to 2.5. Many observations support the conclusion that the diffuse microbands seen inside the dendrite in Figure 3 change into irregularly shaped deformation cells.

The regions between the dendrites, where the particle density is lower, contain well-defined microbands after rolling to a strain of 2.5. The high-angle boundaries observed in regions such as shown in Figure 5 are normally associated with grain boundaries, transition bands or shear bands (17,18). Alternatively, they could be associated with regions of high lattice rotation that have been observed to form at large (> 2 μm diameter) particles in heavily deformed alloys (19). The orientation change across a transition band takes place over a distance of a few micrometers and can be as high as 30° (18). Humphreys (19,20) measured misorientations of the order of 30° at 4 μm diameter silicon particles in aluminum rolled 60%. The observed high-angle boundaries and the micrographs in Figures 2 and 3 suggest that the dendrites produce a complex deformation microstructure in their vicinity which may strongly influence the relaxation behavior during annealing.

4.2 Relaxation Behavior of Al-Zr-Si

The relaxation behavior will be discussed in two parts. This section deals with the hardness data and the optical microscope observations, while the following section addresses the microstructural evolution in terms of boundary misorientations and TEM observations.

Annealing of rolled Al-Zr-Si at progressively higher temperatures leads to more rapid recovery and recrystallization. Lowering the annealing temperature leads to slower relaxation kinetics, but hardness data and metallographic observations show that lower temperatures favor recovery over recrystallization. This is consistent with a higher activation energy for recrystallization than recovery as has been found in previous investigations (21,22).

The competition between recovery and recrystallization is perhaps best illustrated in Section 3.5 for the specimen that was annealed for 72 hours at 350°C prior to being heated slowly to 400°C. The hardness decreased only slightly during the 8 hour anneal at 400°C and this specimen showed less discontinuous recrystallization than an as-rolled specimen that was directly annealed for 8 hours at 400°C. Section 3.5 also showed that a slow heating rate to the annealing temperature allows more recovery to take place and reduces the initial hardness drop during annealing. This is in agreement with the ideas mentioned in the introductory section: when particles retard nucleation, recovery processes have more opportunity to lower the driving pressure for the migration of high-angle boundaries during recrystallization. Extended recovery may eventually preclude nucleation and growth of recrystallized grains.

4.3 Microstructural Evolution of Cold-Rolled Al-Zr-Si

The complex deformation microstructure caused by the dendrites in cold-rolled Al-Zr-Si contains numerous high-angle boundaries where nucleation of new grains can take place during annealing. The high-angle boundaries may induce coalescence of adjacent subgrains which can then form a recrystallization nucleus if the drag pressure from the particles is not sufficiently high. Areas that have a high particle density do not contain high angle boundaries and the particles interfere with the formation of subgrains during recovery.

The fact that the texture of the rolled material did not change appreciably during the 72 hour anneal at 350°C supports the observations made that formation and growth of subgrains is taking place by two processes:

1. By the rearrangement of dislocations into boundaries in areas where there is a homogeneous distribution of dislocations and microbands are absent.
2. By the migration and elimination of boundaries already present in the deformation microstructure.

Figures 11 and 13B shows how microbands in rolled Al-Zr-Si can form subgrains by boundary migration in the short transverse direction (S) and coalescence in the rolling direction (L) during annealing at 350°C. During this stage of recovery, subgrain coalescence is mainly between subgrains that belong to the same microband, such as subgrains 1, 2 and 5 in Figure 13B. The rotations that are necessary for coalescence are small and thus do not create substantially different grain orientations in the microstructure. At higher annealing temperatures, areas such as shown in Figures 11 and 13B would evolve faster and might form a recrystallization nucleus.

Annealing at 375°C for 48 hours leads to a more random texture, which indicates that orientations that are associated with the deformation microstructure are no longer dominating. Figure 16A shows that the transverse orientations of many of the large grains seen in Figure 15 are different from that seen during the initial stages of recovery. Since the volume fraction recrystallized after 48 hours at 375°C is only about 30% (as determined by optical microscopy), it is possible that the microstructure contains many potential nucleation sites such as shown in Figure 15 that have not formed a nucleus but are causing randomization of the texture.

Subgrain coalescence induced by the presence of high-angle boundaries would explain the elongated grains separated by high-angle boundaries seen in Figure 15. It is also in agreement with the suggestion made by Doherty and Cahn (23) that subgrain coalescence should occur preferentially in regions where there is a mixture of low and high angle boundaries. Other areas in the microstructure that have a higher particle density and low misorientation have not yet formed a well defined subgrain structure. These areas contribute to the weak deformation texture components seen in the X-ray pole figure (Figure 10B).

The results described in Section 3.3.2 demonstrate that lowering the annealing temperature leads to slower recrystallization kinetics. At some minimum temperature, no nucleation will take place during annealing and relaxation occurs by recovery processes alone. Annealing rolled Al-Zr-Si at temperatures lower than about 375°C leads to the evolution of a microstructure which is a mixture of recovered regions and discontinuously-recrystallized regions.

4.4 Concurrent Annealing and Deformation of Cold-Rolled Al-Zr-Si

4.4.1 Microstructural Evolution

Concurrent annealing and deformation of rolled Al-0.24Zr-0.1Si leads to a more rapid microstructural evolution than static annealing. This is clearly seen by comparing the microstructure of the deformed and undeformed parts of the tensile specimens. The fact that discontinuous recrystallization takes place in the tensile specimens prior to deformation makes it difficult to judge how much additional discontinuous evolution takes place during deformation. However, extended recovery does take place in the unrecrystallized regions during the initial stages of deformation. The detailed study of the relaxation during static annealing helps to interpret the observations.

After deforming to a strain of 0.22 the microstructure shows high-angle boundaries lying parallel to the tensile direction / rolling direction (Figure 20). A comparison of the microstructure in the gauge section (Figure 20) and in the grip section (Figure 22) shows that the deformation has caused an increase in the subgrain size. The transverse orientations of the subgrains in the gauge section and the corresponding pole-figure (Figure 21) have been seen before during the initial stages of recovery during static annealing. This implies that the subgrains have coarsened by a rearrangement of boundaries that are present prior to concurrent annealing and deformation. Some examples of boundary coalescence can be seen in Figure 20. The driving pressure for boundary migration is both the reduction in defect density and the applied stress felt by the boundaries.

The numerous dislocations observed after a strain of 0.22 indicate that a dislocation creep mechanism is responsible for at least some of the strain.

Figure 20 shows that particles are retarding the movement of some of the boundaries. The boundaries have caused dissolution of some of the small Al_3Zr particles, leading to subsequent precipitation of large incoherent Al_3Zr particles on the boundaries. As the particles coarsen on the boundaries, the drag pressure decreases so the boundary can escape if the driving pressure is sufficiently high. This leaves a row of particles behind the boundary. This has been observed in both Al-Zr (15) and Al-Mn alloys (16). Figure 20 shows some examples where boundaries have escaped from particles.

Further deformation to a strain of 0.46 is accompanied by a slight decrease in flow stress and the appearance of small grains in those areas that are not discontinuously recrystallized prior to deformation. The transverse orientations of the grains and subgrains observed in the microstructure are similar to those seen after a strain of 0.22, but the misorientations between adjacent grains is greater. This is reflected in the greater separation of poles in the pole figure. These observations suggest that the microstructure seen after deformation to a strain of 0.46 has been formed by the rearrangement of boundaries that are present in the microstructure prior to deformation.

4.4.2 Comparison of Al-0.24Zr-0.1Si and SUPRAL

One purpose of this study is to gain a better understanding of the role that Al_3Zr particles play in superplastic Zr-bearing aluminum alloys. The commercial superplastic alloy SUPRAL (Al-6Cu-0.5Zr) shows extended recovery (4,24,25) during the initial stages of the superplastic forming process.

Deformation of SUPRAL at 450°C using a strain rate of 3.3×10^{-3} s^{-1} gives rise to a continuous evolution of a subgrain structure to a grain structure during the initial 50 % elongation. It must be noted that the term "grain size" used in this section applies both to subgrains and grains. This convention is used extensively in the study of superplasticity and dynamic recrystallization. Observation of a continuous range of microstructures in the present study has shown that many phenomena which lie on the borderline of classical definitions may occur when the drag pressure from particles is approximately equal to the driving pressure for recrystallization. Figure 23 shows the grain size and misorientation as a function of strain for the Al-0.24Zr-0.1Si and SUPRAL. The more gradual increase in grain size with increasing strain at a higher temperature (450°C) shows that the SUPRAL alloy has a higher particle drag pressure. The misorientation plot shows an increase in the average misorientation in both cases. The range bars on the data points from this study indicate the wide range of misorientations which was observed.

Perhaps the most important difference between these alloys, aside from drag pressure, is the microstructure that is present prior to deformation. Nes (4) reports that prior to deformation the misorientations in SUPRAL are low (1 - 2°) in the partially recovered deformation microstructure and that the subgrains / grains remain equiaxed during deformation. Concurrent annealing and deformation of SUPRAL does not appear to change the texture in terms of producing new texture components (4,25). The strength of the main texture components do however change with strain and it has been attributed to grain boundary sliding (25). A majority of experimental data suggests that grain boundary sliding is the dominant mechanism in the superplastic deformation process (26). In the Al-Zr-Si alloy studied here, the deformation microstructure is far from being homogeneous and the data presented here show that this influences the evolution of microstructure during static and dynamic annealing. The high-angle boundaries seen after deformation to a strain of 0.22 have a high enough misorientation for grain boundary sliding (27). The elongated shape of the subgrains in the Al-Zr-Si alloy after a strain of 0.22 makes it hard for them to rotate to accommodate grain boundary sliding (27).

An additional difference between SUPRAL and the Al-Zr-Si alloy is composition. Many workers have speculated on the observed beneficial effects of ternary additions to Al-Zr in terms of superplastic properties. According to Bricknell and Edington (24), the suggestion of Watts et al. (28) best explains the role of Cu. Their observations showed that Cu provides a more uniform Zr distribution on casting and that Al_2Cu particles can provide a boundary drag pressure in areas depleted of Zr. However, quantitative results are lacking and this explanation remains speculative.

5. SUMMARY

In summarizing progress during the past year, it is convenient to refer to the basic questions about extended recovery that appeared near the end of the introduction section.

1. Does concurrent annealing and deformation introduce new mechanisms of microstructure relaxation that are not available by annealing alone? Results of this investigation show that polygonization, subgrain boundary migration, and possibly subgrain coalescence are the basic mechanisms of recovery with or without concurrent deformation; deformation does not introduce new mechanisms. This conclusion is supported by the texture analysis results and by TEM observations of the microstructure. This conclusion suggests that "extended recovery" is a more appropriate term for this process than "continuous

recrystallization", since only recovery mechanisms operate.

2. What features of the microstructure play key roles in the extended recovery process? The two features that appear to be most important are the dispersoid particle distribution and dislocation cell or microband boundaries that are present in the deformation substructure. A more homogeneous dispersoid particle distribution is better able to suppress discontinuous recrystallization because the boundary drag pressure is approximately uniform. However, the presence of boundaries with moderate misorientations in the deformation substructure is also an important feature for extended recovery and it appears that an inhomogeneous distribution of dispersoid particles is more beneficial in this regard. By selecting a suitable temperature for concurrent deformation and annealing, an moderately inhomogeneous dispersoid particle distribution can be tolerated without excessive discontinuous recrystallization.

3. By what mechanism does concurrent deformation speed-up recovery? Only part of the answer to this question is clear: no new mechanisms are introduced by concurrent deformation. Several previous investigators have suggested that straining introduces geometrical effects which promote more rapid subgrain boundary migration. Theoretical analyses (not described in this report) suggest that this explanation is incorrect. The alternative explanation, stress-assisted boundary migration, has not been considered by previous investigators. A model for stress assisted boundary migration is currently being formulated and results will be contained in a subsequent report.

6. REFERENCES

1. R.D. Doherty, Metal Science, 8, (1974), pp.132-142.

2. H. Alborn, E. Hornbogen and U. Koster, J. Mat. Sci., 4,(1969) 944-950.

3. J.W. Martin and R.D. Doherty, Stability of Microstructure in Metallic Systems, Cambridge University Press, Cambridge, 1976, pp. 150-153.

4. E. Nes, "Continuous Recrystallization and Grain Growth during Superplastic Flow", in Superplasticite/Superplasticity, B. Baudelet and M. Suery (eds.), Editions du CNRS, Paris, 1985, pp. 7.1 - 7.11.

5. R. Grimes, M.J. Stowell and B.M. Watts, Metals Technology, 3 (1976) 154-160.

6. C.J. Tweed, B. Ralph and N. Hansen, Acta Met., 32, (1984), 1407-1414.

7. E. Nes, Acta Met., 20, (1972), pp. 499-506.

8. N. Hansen, Constitution of Binary Alloys, McGraw-Hill, 1958, p.152.

9. O. Reiso, H. Westengen, L. Auran,"Effect of Si Additions on Precipitation and Recrystallization in Al-0.18wt% Zr alloys", 7th Light Metals Congress, Leoben, Vienna, (1981), pp. 186-188.

10. M.S. Zedalis and M.E. Fine, Met. Trans., 17A, (1986), pp. 2187-2198.

11. L.F. Murr, Interfacial phenomena in Metals and Alloys, Addison-Wesley, Reading, 1975, p. 131.

12. E. Nes, N. Ryum and O. Hunderi, Acta Met., 33, (1985),pp. 11-22.

13. R.D. Doherty, "Nucleation of Recrystallization in Single Phase and Dispersion Hardened Polycrystalline Materials," 1st Riso Int. Symp. on Metallurgy and Materials Science, Roskilde, Denmark, 1980, pp. 57-69.

14. H. Hu, "Recovery, Recrystallization and Grain Growth", in Metallurgical Treatises, J.K. Tien and J. F. Elliot, (eds.), The Metallurgical Society of AIME, Warrendale, PA, 1981, pp. 385-407.

15. E. Nes, Metal Science,13, (1979), 211-215.

16. D.B. Goel, P. Furrer and H. Warlimont, ALUMINUM 50, (1974), p. 511

17. M. Hatherly, "Deformation at High Strains", 6th. International Conference on the Strength of Metals and Alloys, R.C. Gifkins (ed.), Pergamon Press, Oxford, 1982, pp. 1181-1195.

18. A.R. Jones, B. Ralph and N. Hansen, Proc. Roy. Soc., 368A, (1979), pp. 345-357.

19. F.J. Humphreys, Acta Met., 25, (1977), 1323-1344.

20. F.J. Humphreys, Metal Science, 13 (1979) 136-145.

21. R.A. Vandermeer, P. Gordon, "The Influence of Recovery on Recrystallization in Aluminum", in Recovery and Recrystallization of Metals, L. Himmel (ed.), Interscience, New York, 1963, p. 211

22. R. Kaspar, J. Pluhar, Metal Science,9, (1975), pp. 104-110.

23. R.D. Doherty and R.W. Cahn, J. Less-Common Metals, 28, (1972), pp. 279-296.

24. R.H. Bricknell and J.W. Edington, Met. Trans., 10a, (1979), pp. 1257-1263.

25. R.H. Bricknell and J.W. Edington, Acta Met., 27, (1979), pp. 1303-1311.

26. A. Arieli and A.K. Mukherjee, Met. Trans.,13A, (1982), pp. 717-732

27. O.D. Sherby and J. Wadsworth, "Development and Characterization of Fine-Grain Superplastic Materials" in Deformation, Processing, and Structure, George Krauss (ed.), American Society for Metals, Metals Park, Ohio, 1984.

28. B.M. Watts, M.J. Stowell, B.L. Baikie and D.G.E. Owen, Metal Science, 10, (1976) pp. 198-206.

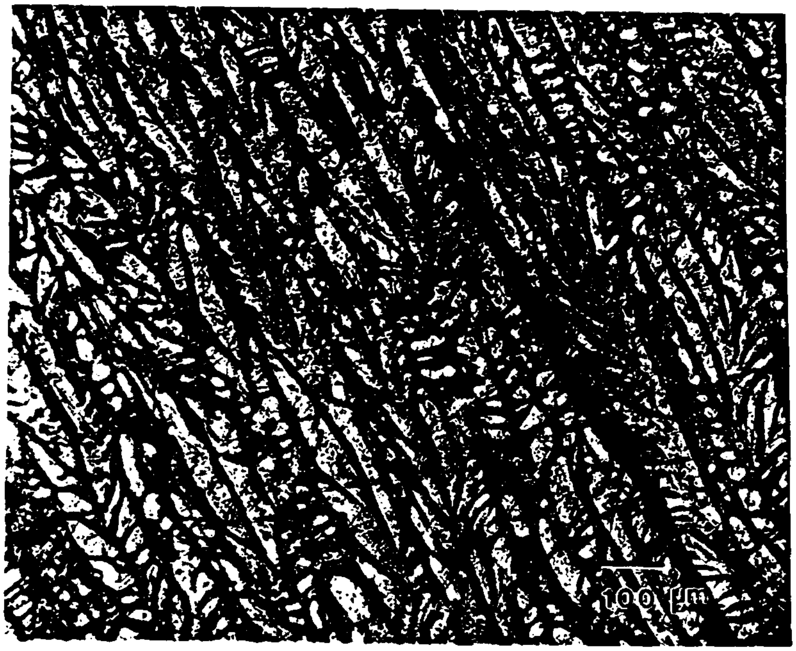

Figure 1. Optical micrograph showing cellular segregation of Zr in a heat-treated Al-Zr-Si specimen. Section normal to the transverse direction. Etched 3 minutes in a NaOH-H_2O solution.

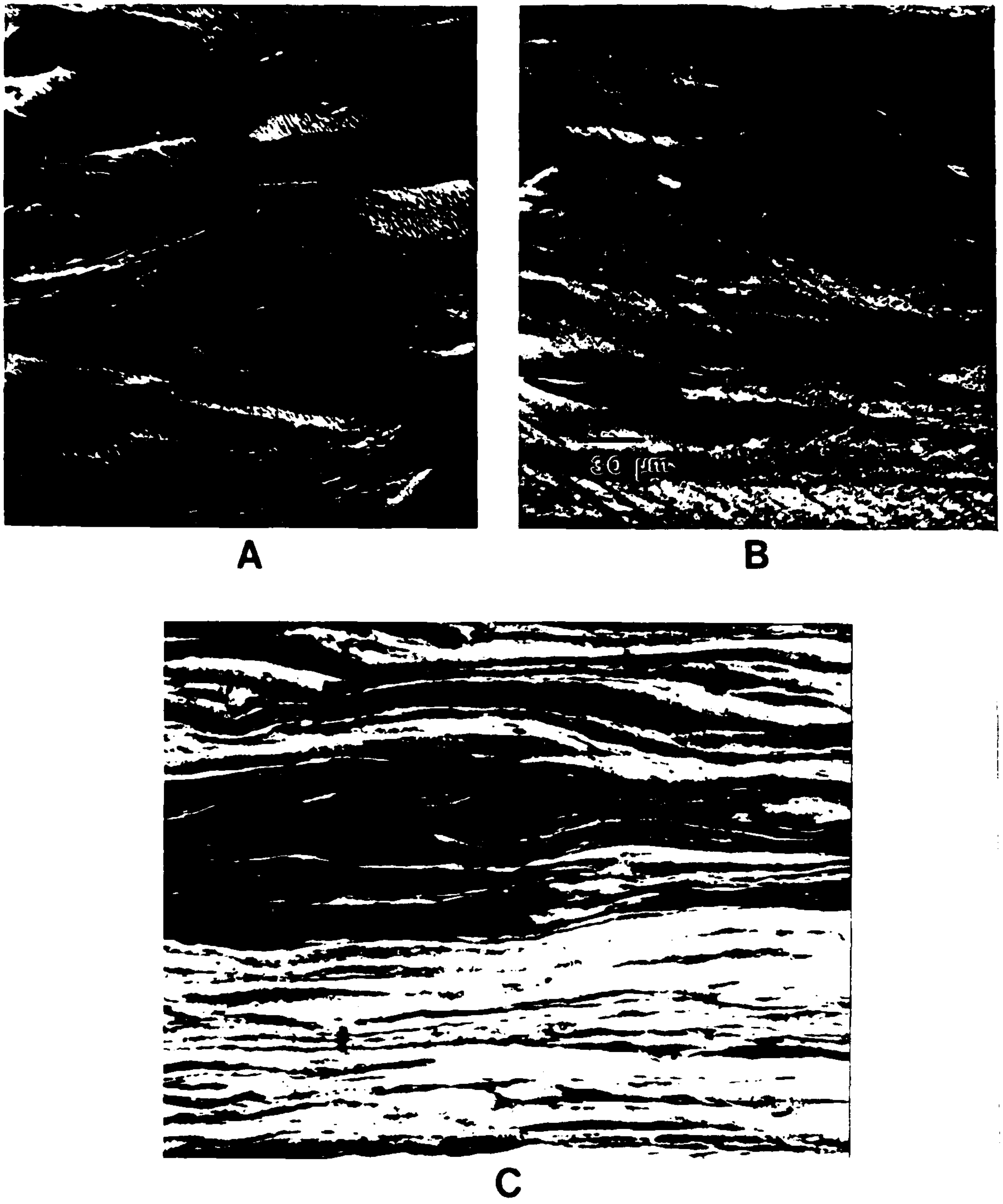

Figure 2. Optical micrographs of sections normal to the transverse direction in Al-0.24%Zr-0.1Si cold-rolled to an effective strain of A) 0.9, B) 1.5, C) 2.5. Anodized with Barkers etch.

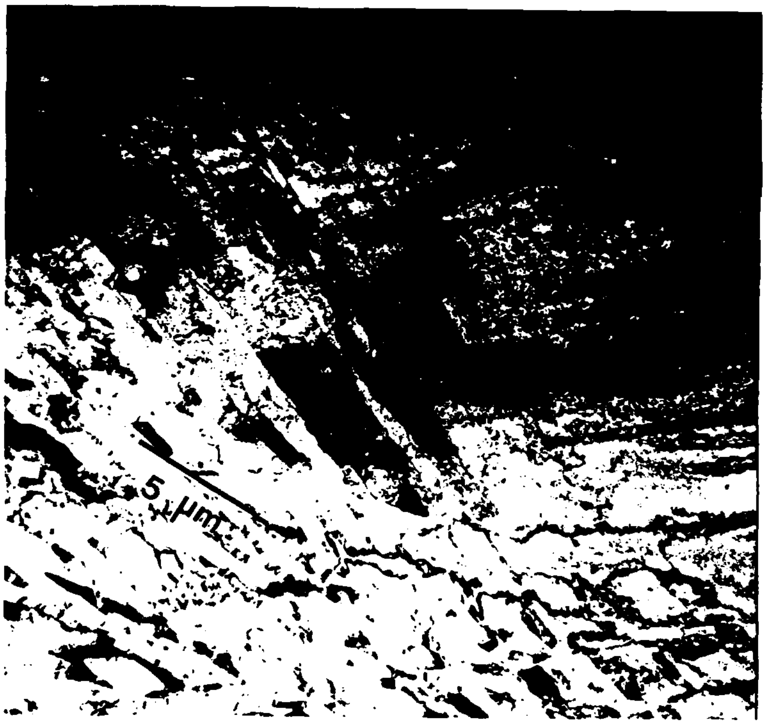

Figure 3. TEM micrograph of Zr rich area in Al-0.24Zr-0.1Si cold-rolled to an effective strain of 1.5. The section is normal to the transverse direction. The micron marker is parallel to the rolling direction.

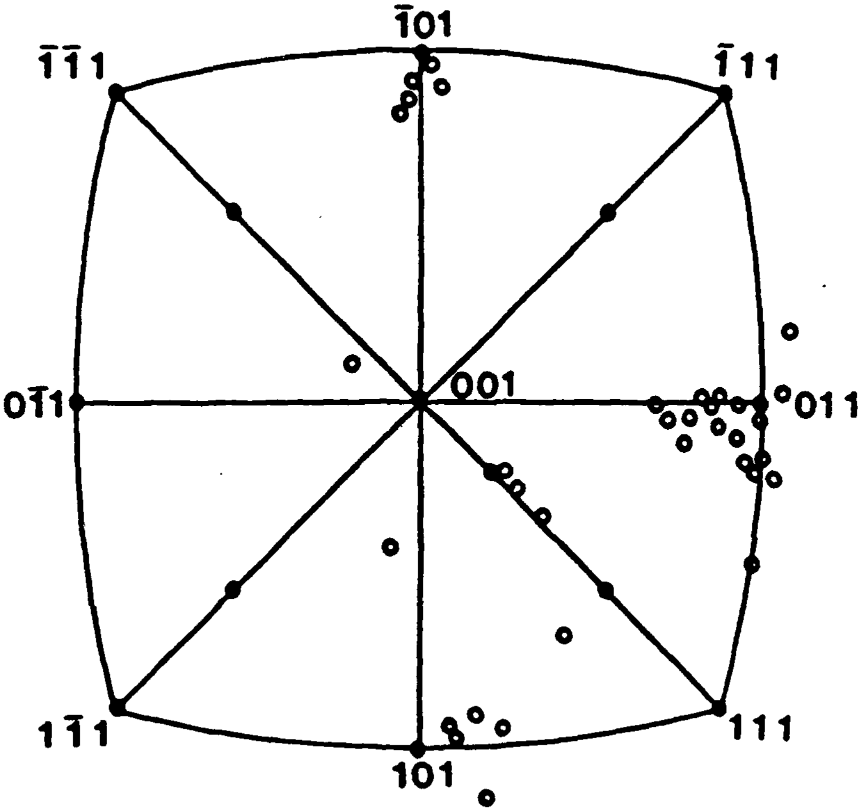
$\bar{1}01$
$\bar{1}\bar{1}1$
$\bar{1}11$
$0\bar{1}1$
001
011
$1\bar{1}1$
111
101

Figure 4. Transverse orientations of selected microbands in Al-0.24Zr-0.1Si cold-rolled to an effective strain of 2.5.

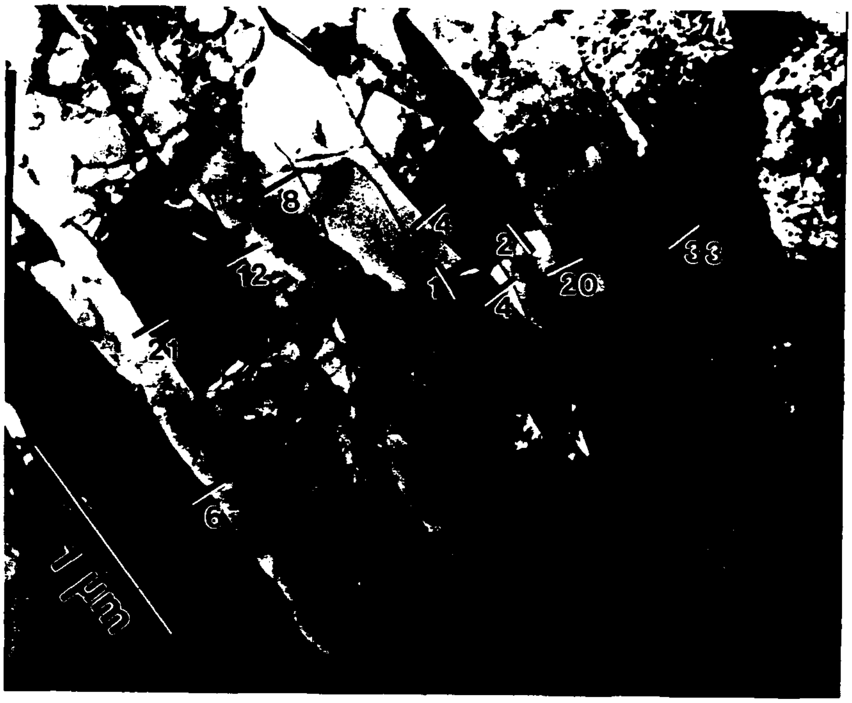

Figure 5. TEM micrograph of region of high misorientations in Al-0.24Zr-0.1Si cold-rolled to an effective strain of 2.5. Section normal to the transverse direction. Misorientations in degrees.

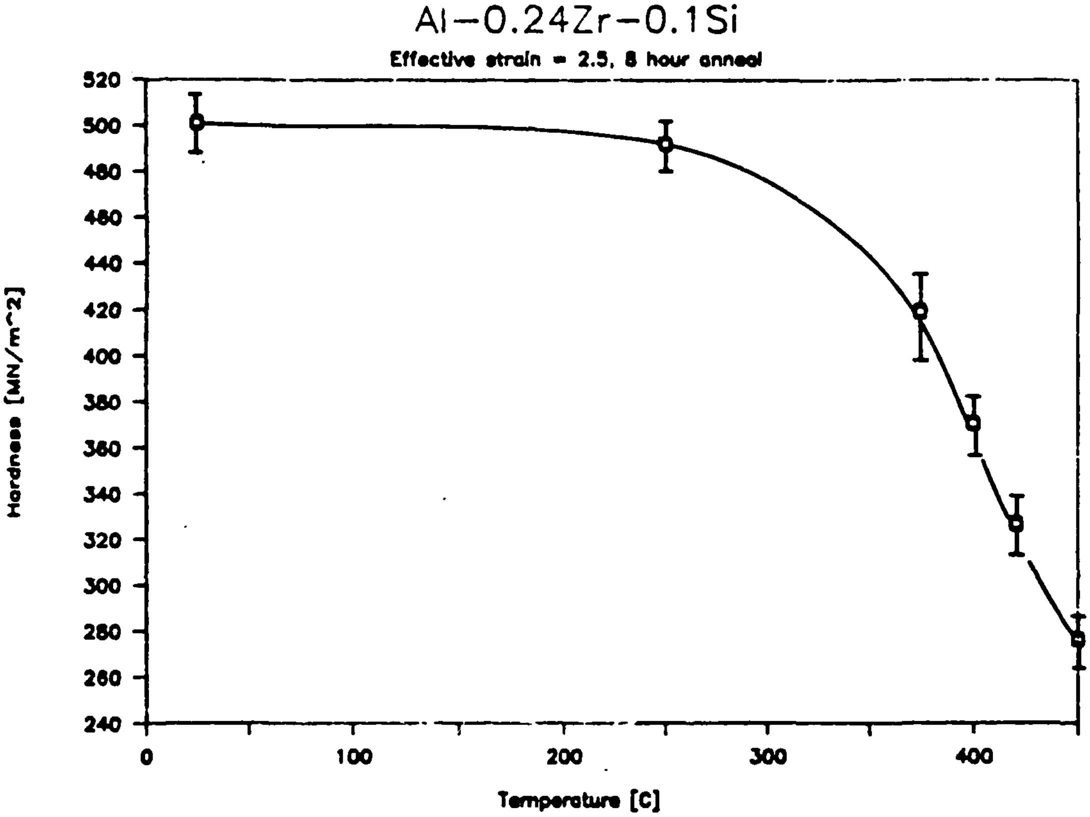

Figure 6. Al-0.24Zr-0.1Si cold-rolled to an effective strain of 2.5. Microhardness as a function of annealing temperature for an 8 hour anneal.

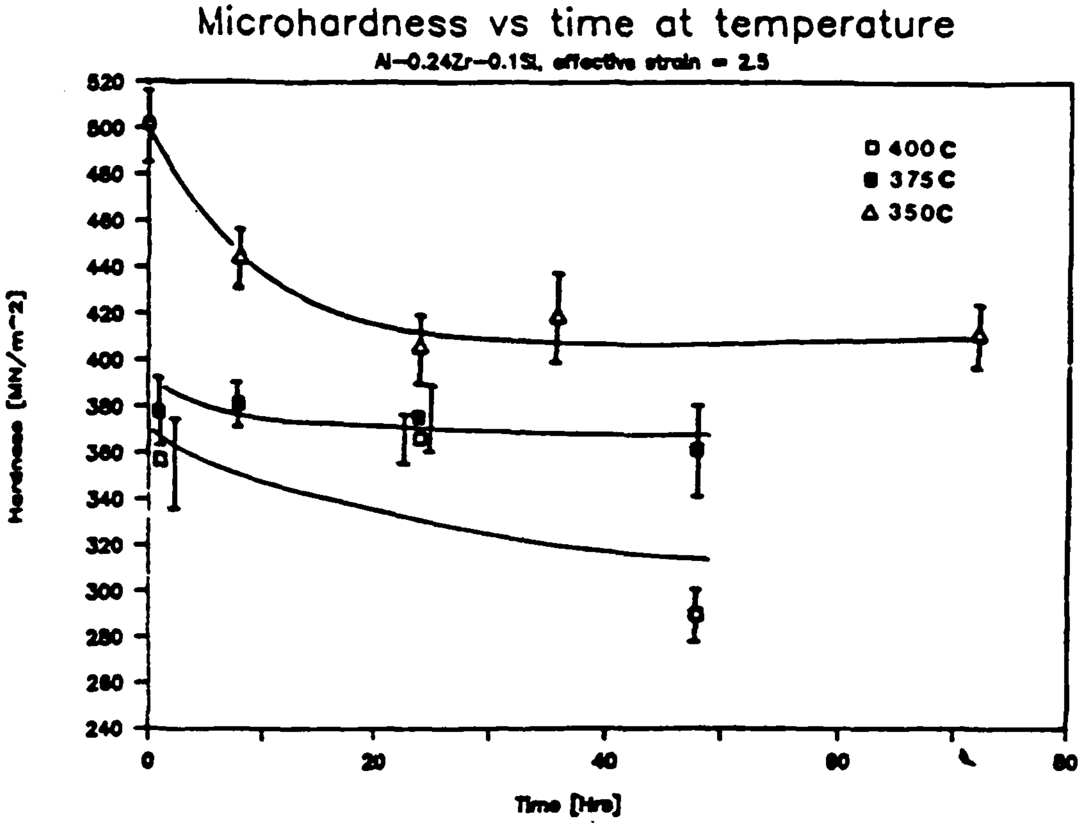

Figure 7. Microhardness as a function of time for Al-0.24Zr-0.1Si cold-rolled to a strain of 2.5 for three different annealing temperatures: 350°C, 375°C, 400°C. Microhardness of as rolled material = (502±15) kgf/mm^2.

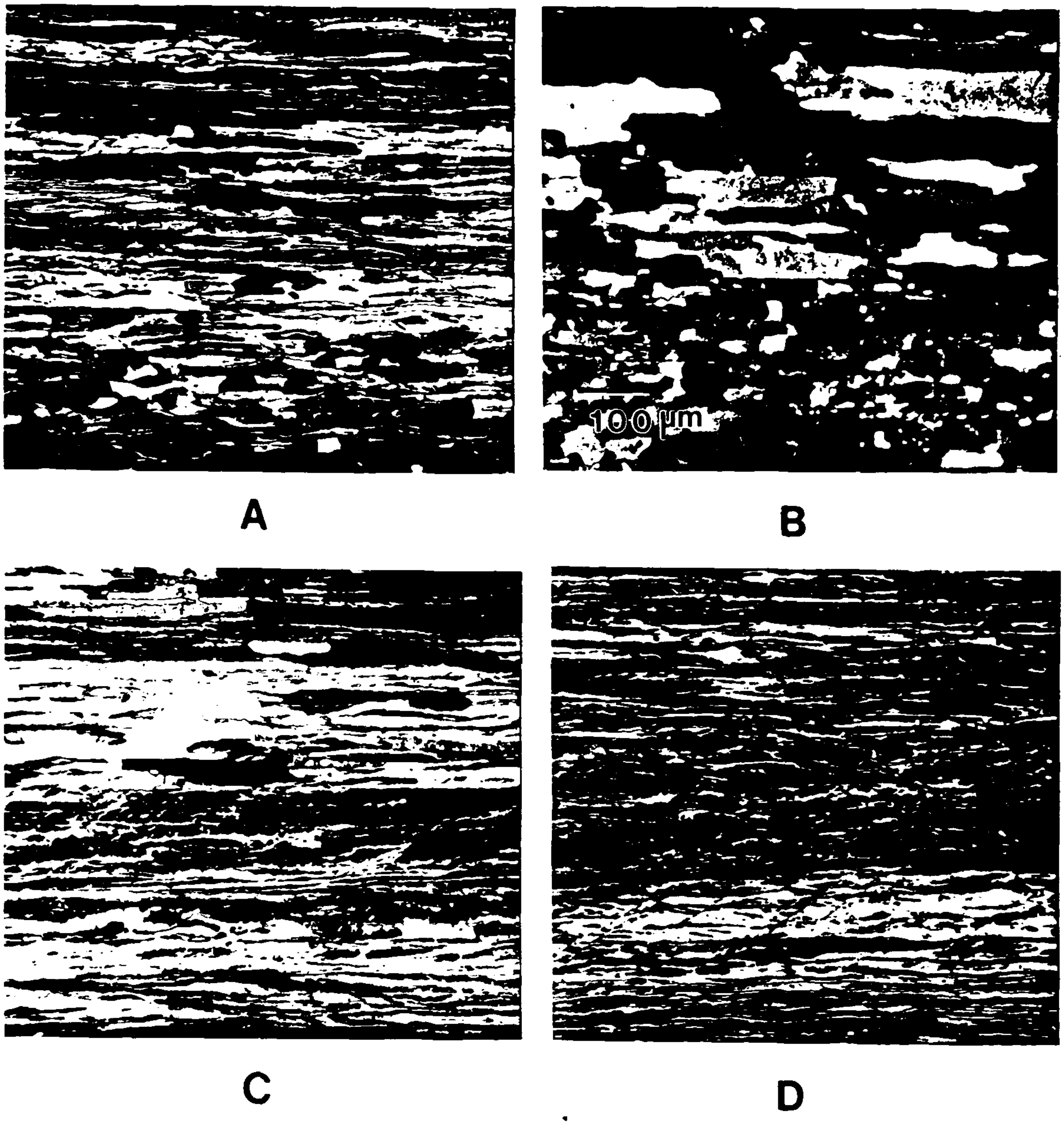

Figure 8. Optical micrographs normal to the transverse direction in Al-0.24Zr-0.1Si cold-rolled (effective strain = 2.5) and subsequently annealed: A) 400°C/15 minutes, B) 400°C/48 hours, C) 375°C/48 hours, D) 350°C/72 hours.

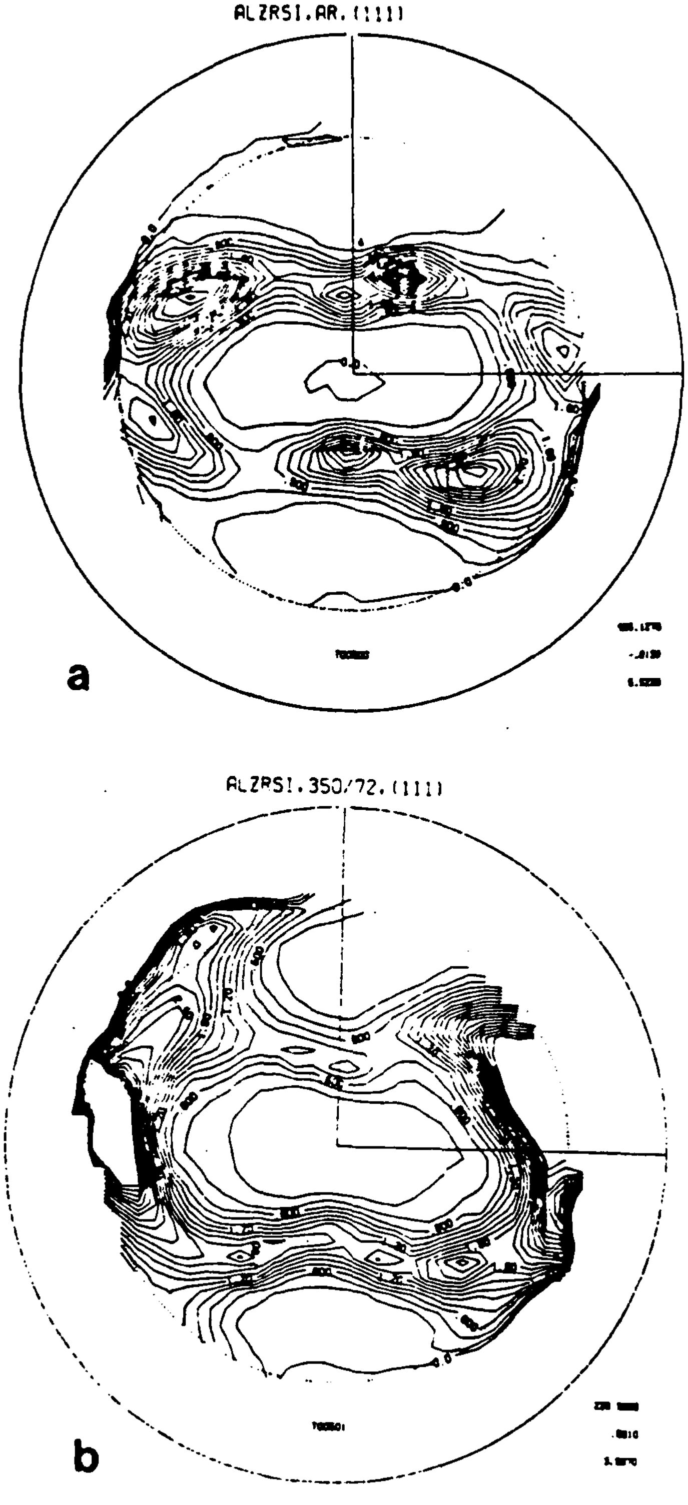

Figure 9. A) Partial (111) pole figure for as-rolled Al-0.24Zr-0.1Si. B) Partial (111) pole figure for a specimen that was rolled and then annealed for 72 hours at 350°C.

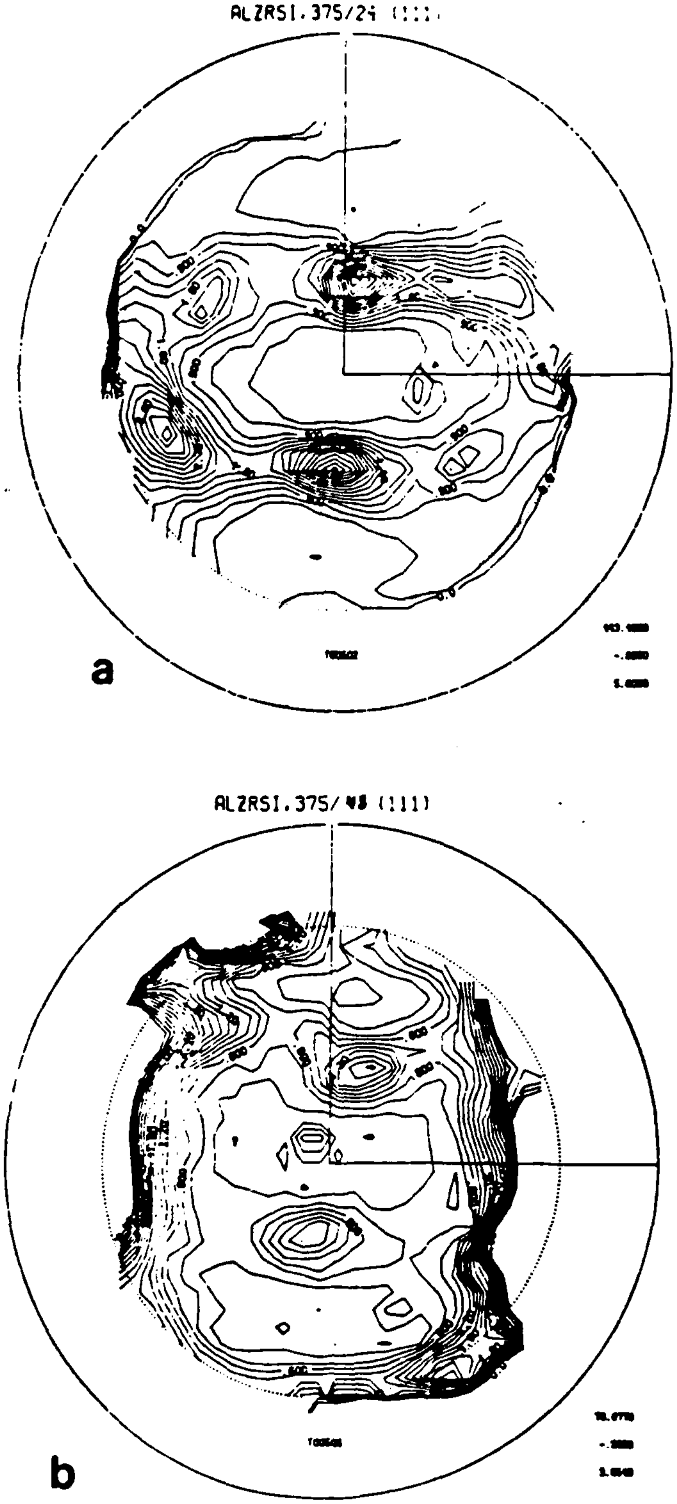

Figure 10. Partial (111) pole figures for cold-rolled Al-0.24Zr-0.1Si annealed at 375°C for: A) 24 hours, B) 48 hours.

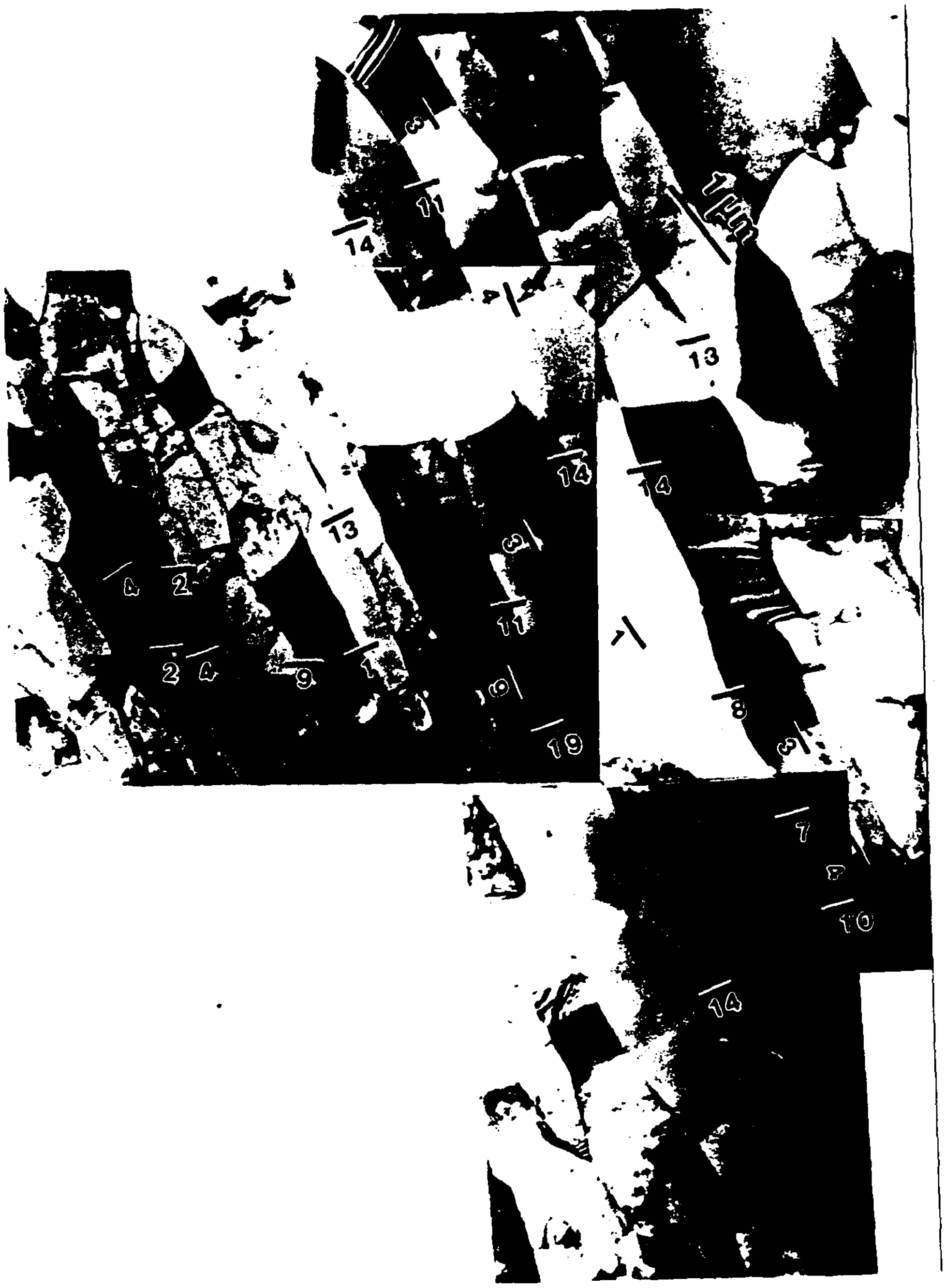
1µm
8
11
14
13
14
14
13
4
2
2
4
9
1
8
11
19
8
8
7
10
14

Figure 11. TEM micrographs of region in cold-rolled Al-0.24Zr-0.1Si after an 8 hour anneal at 350°C. Section normal to the transverse direction. Misorientations between subgrains are shown in degrees.

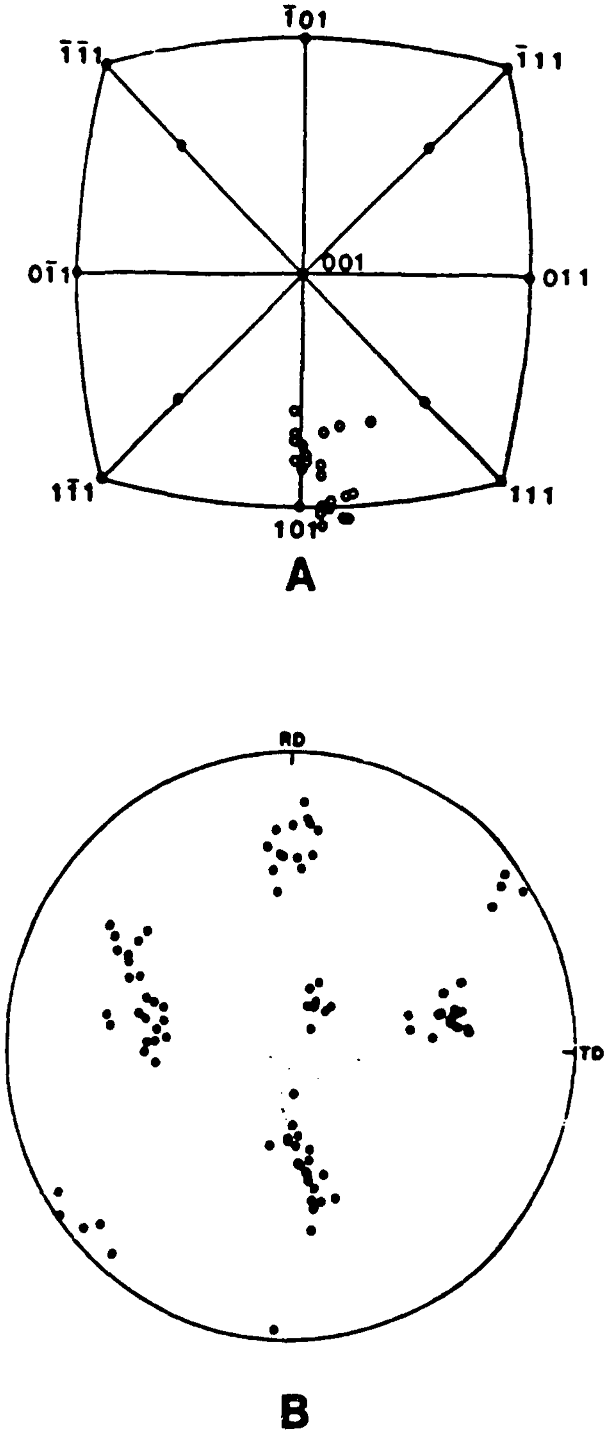

Figure 12. A) Transverse orientations of subgrains in Figure 22 (350°C/ 8 hours). B) (111) pole figure generated for the orientations in (A)

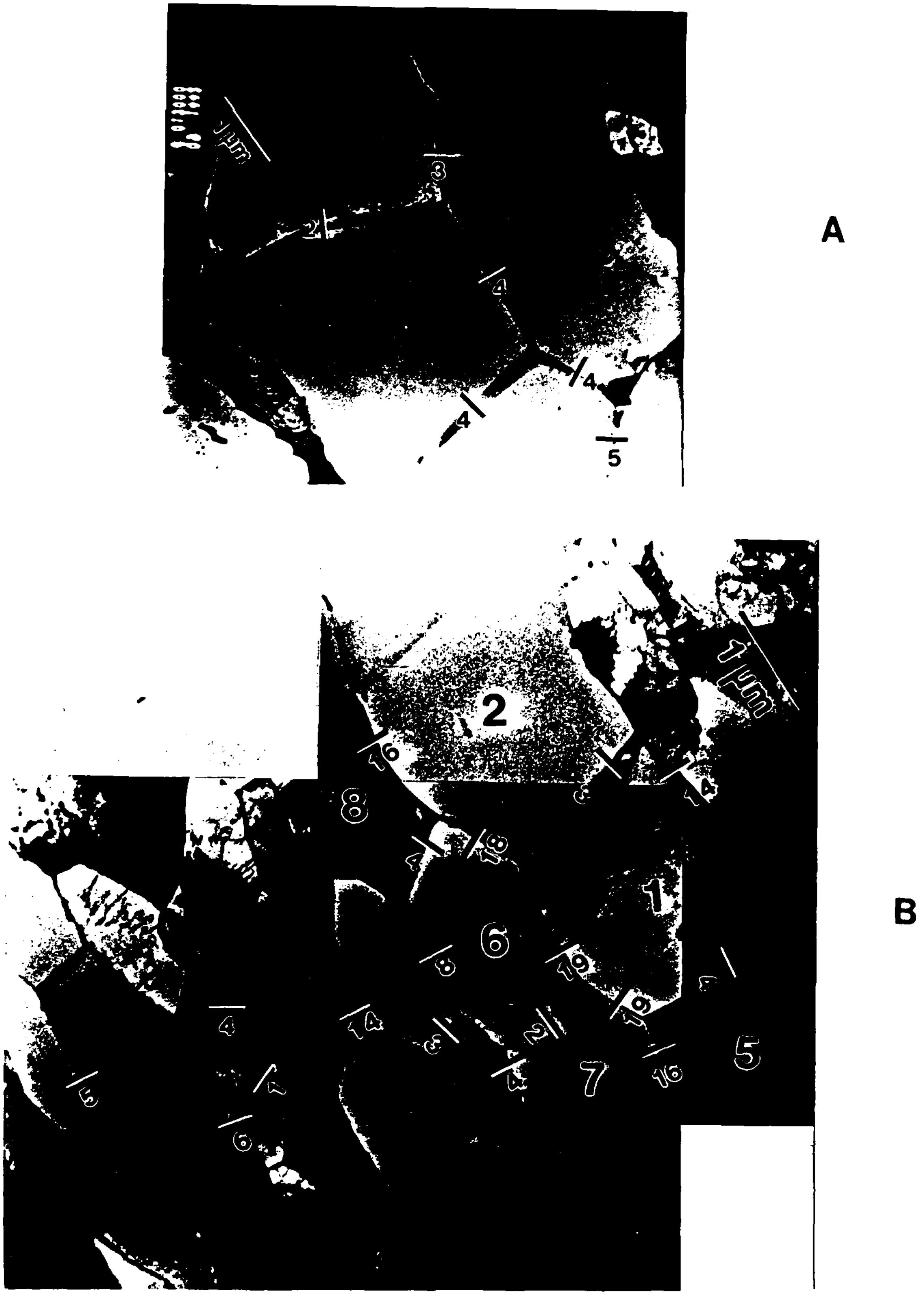

A
1μm
2
3
4
4
4
5
B
1μm
2
16
8
14
8
4
18
1
6
8
19
19
4
14
8
2
4
7
16
5
5
6

Figure 13. A) and B): TEM micrographs of two areas in Al-0.24Zr-0.1Si cold-rolled and subsequently annealed for 72 hours at 350°C. Misorientations in degrees.

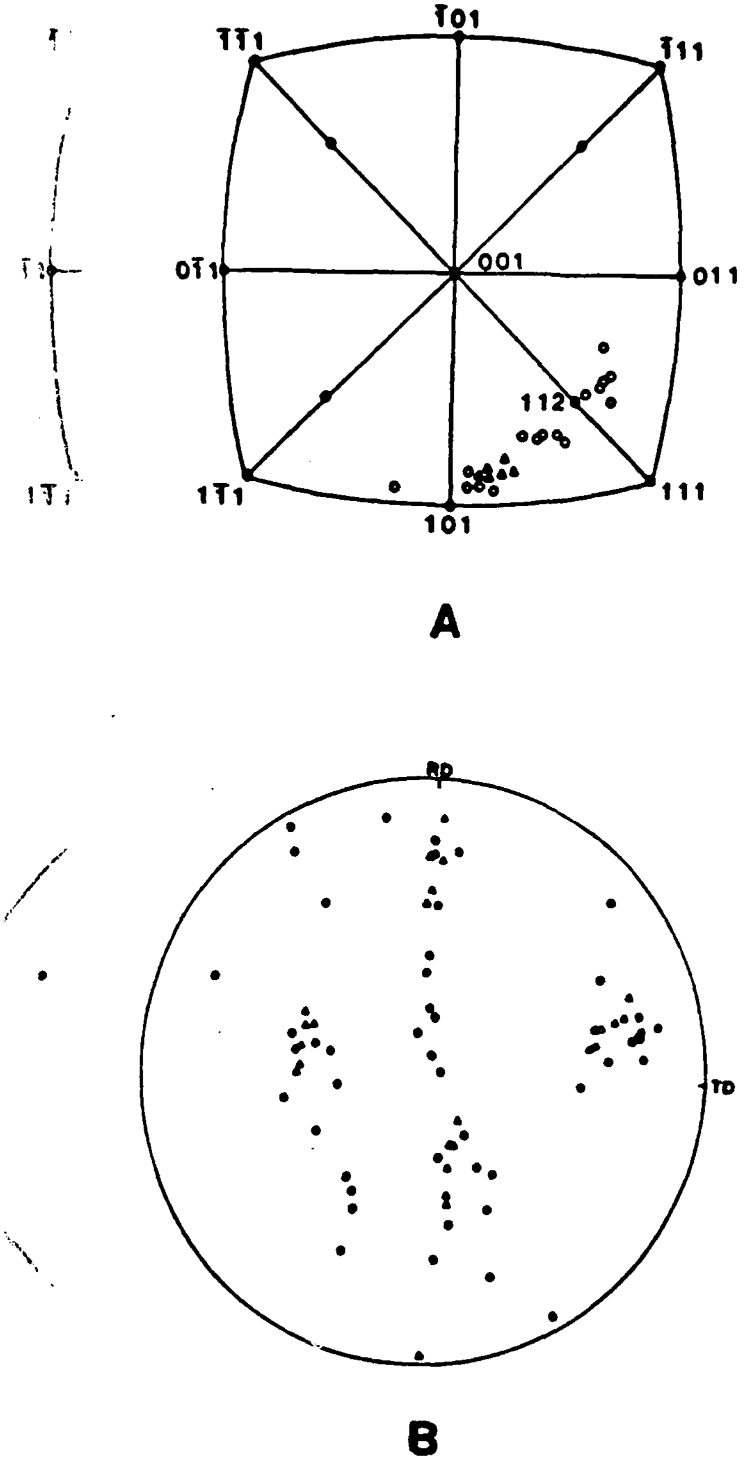

Figure 14. A) Transverse orientations of subgrains in Figure 14 (350°C/ 72 hours). B) (111) pole figure generated from the orientations in (A).

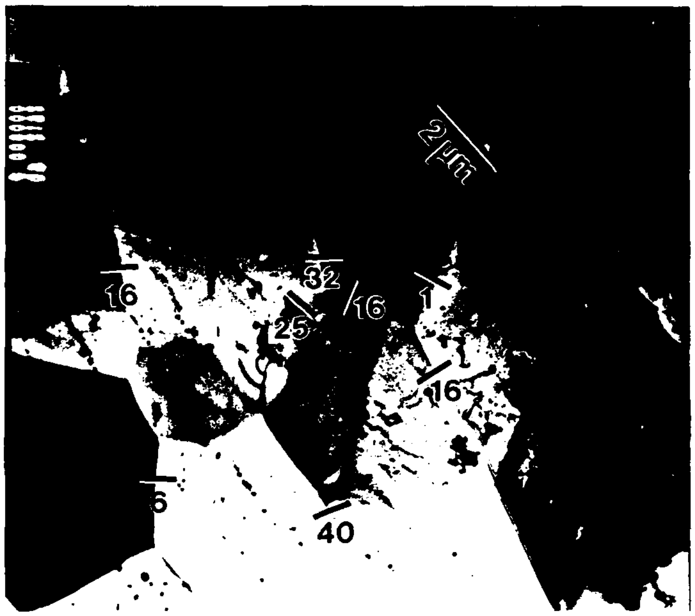
2 µm
16
32
16
25
1
16
6
40

Figure 15. TEM micrograph of Al-0.24Zr-0.1Si cold-rolled and subsequently annealed at 375°C for 48 hours.

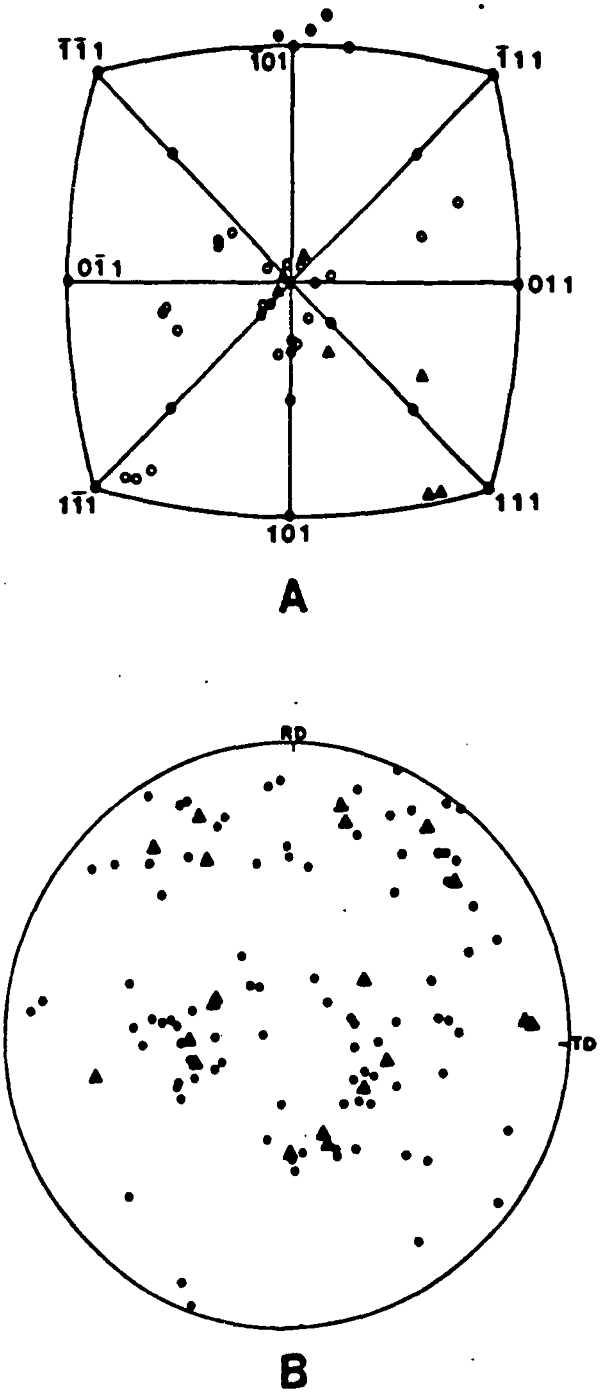

Figure 16. A) Transverse orientations of subgrains shown in Figure 15 (Δ) and from other micrographs (o). B) (111) pole figure generated from the orientations in (A)

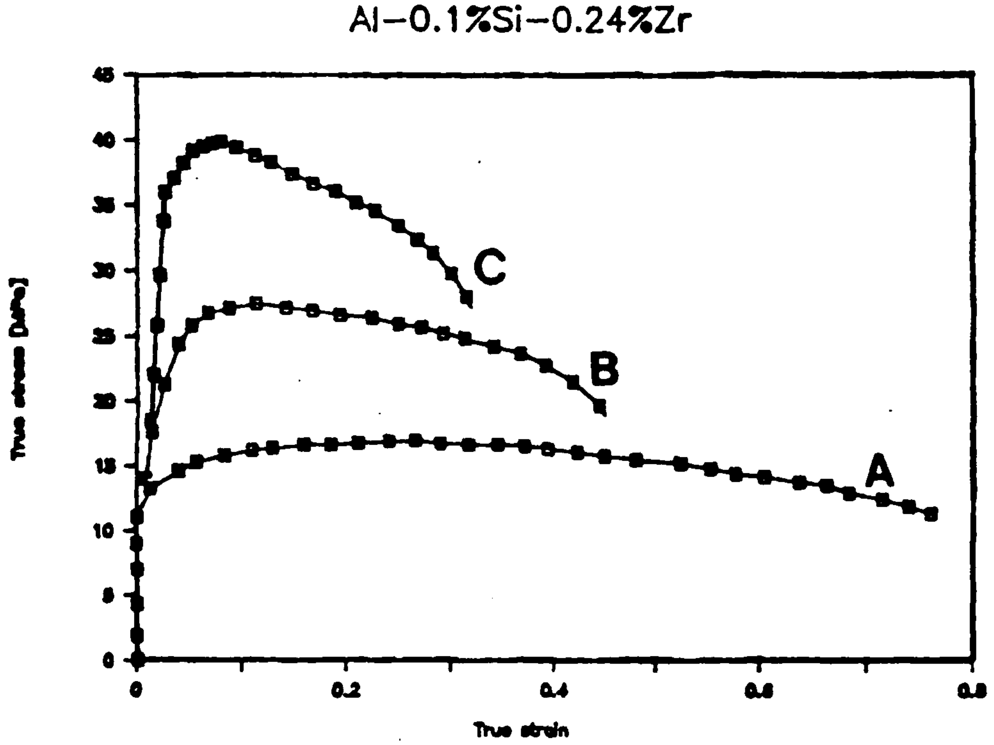

Figure 17. True stress - true strain curves for cold- rolled Al-0.24Zr-0.1Si tested at three different strain rates at 400°C. A) $6.5\text{x}10^{-4}$ s^{-1}, B) $6.5\text{x}10^{-3}$ s^{-1}, C) $6.5\text{x}10^{-2}$ s^{-1}

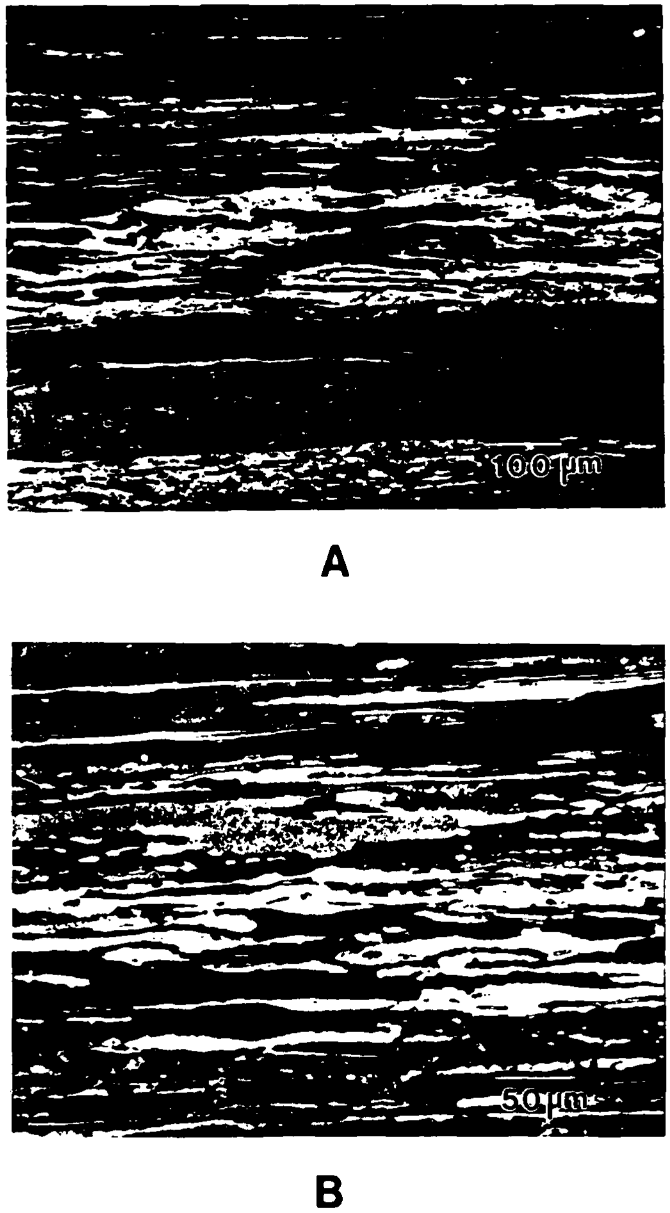

Figure 18. Optical micrographs from cross-sections normal to the transverse direction from an Al-0.24Zr-0.1Si tensile specimen tested to a strain of 0.22: A) Undeformed grip section, B) Deformed gauge section.

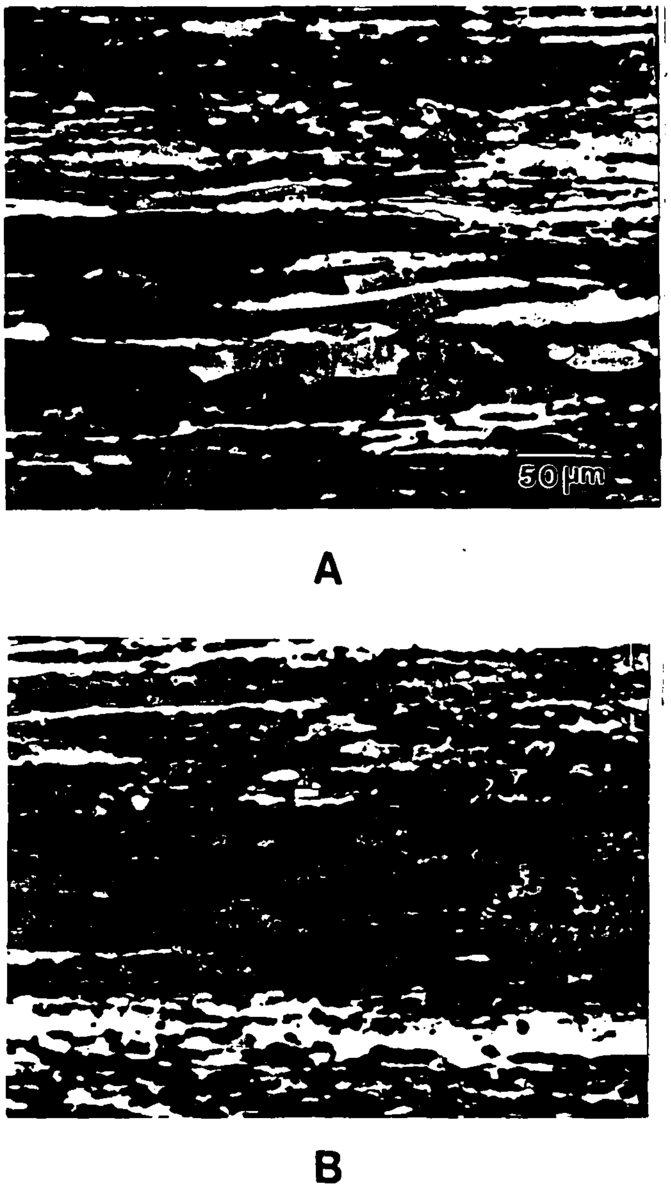

Figure 19. Optical micrographs from cross-sections normal to the transverse direction from Al-0.24Zr-0.1Si tensile specimen tested to a strain of: A) 0.46, B) 0.76.

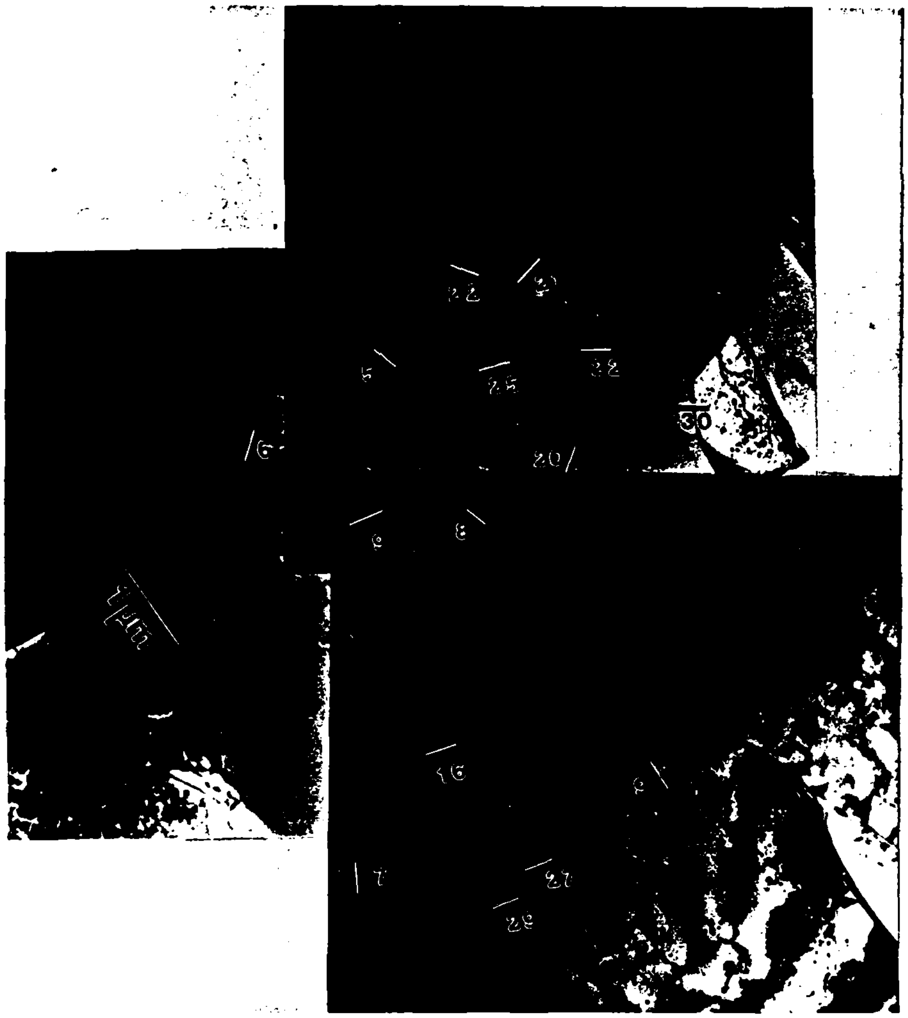
22
5
25
32
30
6
20
9
8
1 μm
16
7
27
29

Figure 20. TEM micrograph of an area in the deformed section of an Al-0.24Zr-0.1Si tensile specimen tested to a strain of 0.22.

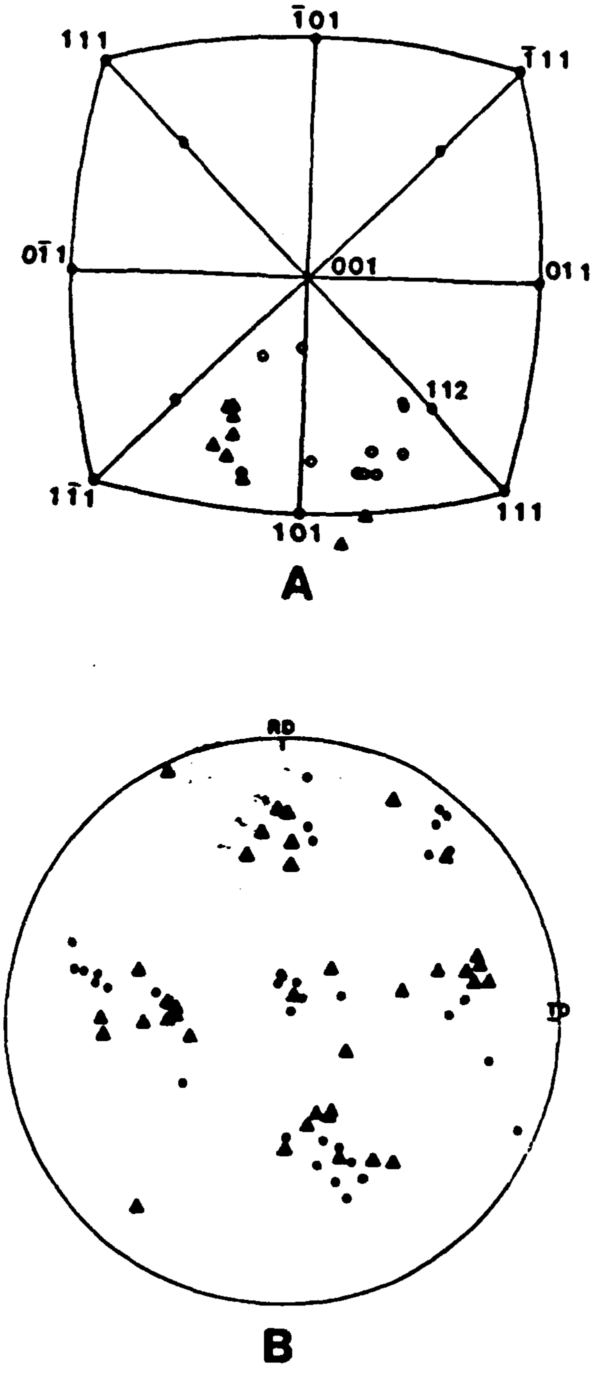

Figure 21. A) Transverse orientations of subgrains in Figure 20. B) (111) pole figure generated for the orientations in (A). The markings for the poles correspond to the marked orientations in (A).

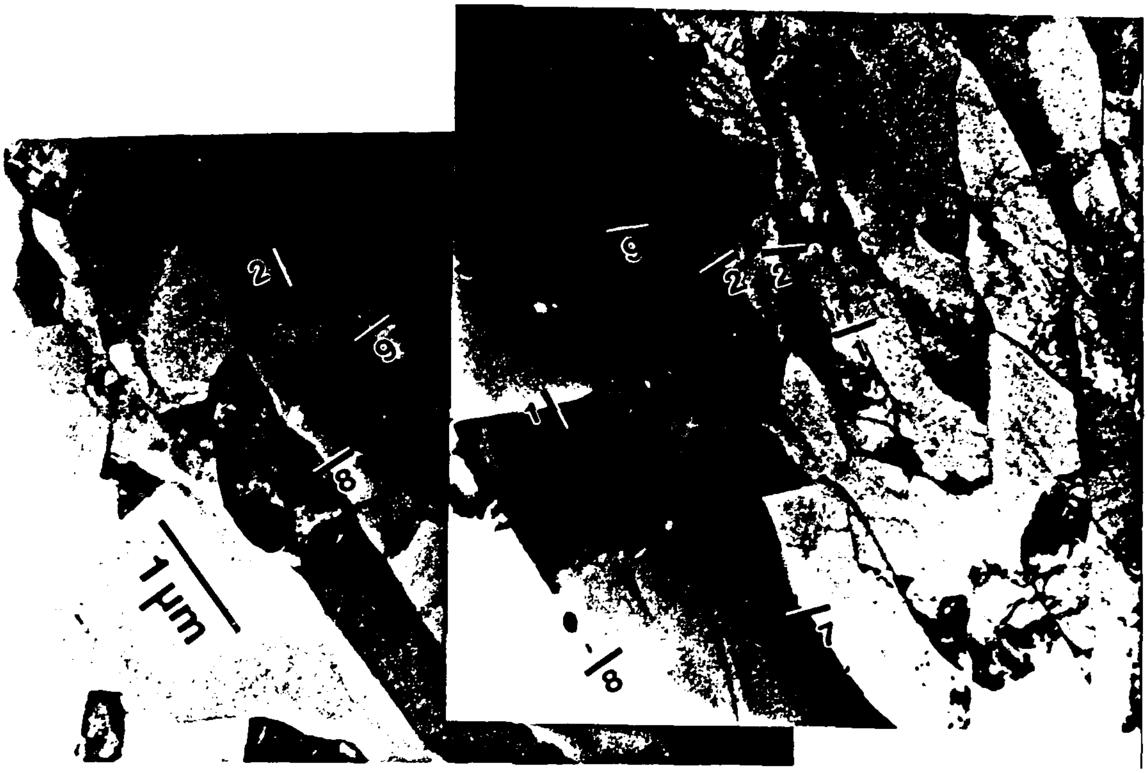
2
6
8
1 µm
3
2
2
1
1
8
7

Figure 22. A) TEM micrograph of an area in the undeformed grip section of an Al-0.24Zr-0.1Si tensile specimen tested to a strain of 0.22.

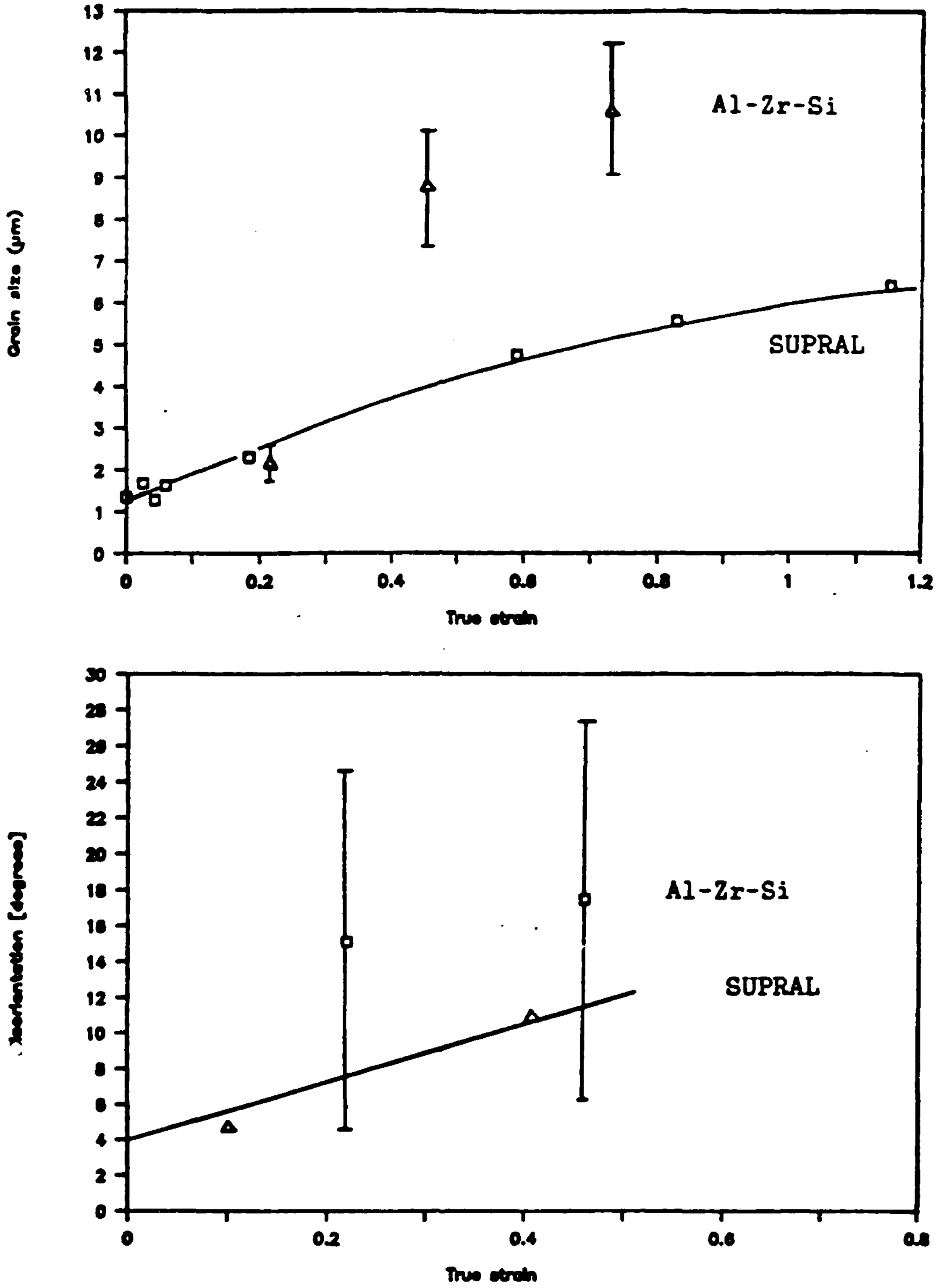

Figure 23. Boundary misorientation and grain size as a function of strain for Al-0.24Zr-0.1Si and SUPRAL (from reference (4)).

DISTRIBUTION LIST

1 - 6	Air Force Office of Scientific Research Building 410 Bolling Air Force Base Washington, DC 20332 Attention: Dr. Alan H. Rosenstein
7 - 8	J. A. Wert, MS
9	T. H. Courtney, MS
10	E. A. Starke, UVa.
11 - 12	Ms. E. H. Pancake, Clark Hall
13	SEAS Pre-award Administration Files

JO# 2259:ph